J. Fluid Mech. (2026), *vol.* 1035, A12, doi:10.1017/jfm.2026.11546

Beyond the Reynolds analogy: bubble-induced modulation of turbulent heat transfer

Davide Procacci[1,2], **Simone Di Giorgio**[3,2], **Alfredo Soldati**[2,4] and **Jannike Solsvik**[1]

[1]Department of Chemical Engineering, Norwegian University of Science and Technology (NTNU), 7491 Trondheim, Norway

[2]Institute of Fluid Mechanics and Heat Transfer, TU Wien, 1060 Vienna, Austria

[3]Istituto di Ingegneria del Mare, Consiglio Nazionale delle Ricerche (INM-CNR), Via di Vallerano 139, Rome 00128, Italy

[4]Polytechnic Department of Engineering and Architecture, University of Udine, 33100 Udine, Italy

Corresponding authors: Davide Procacci, davide.procacci@ntnu.no; Jannike Solsvik, jannike.solsvik@ntnu.no

(Received 3 October 2025; revised 24 February 2026; accepted 9 April 2026)

Boiling and bubble injection are effective strategies for enhancing heat transfer between solid boundaries and a working fluid in numerous industrial applications, including nuclear reactors and molten metal processing. Motivated by this, we conduct direct numerical simulations of a vertical, turbulent, differentially heated, bubble-laden channel flow. The Prandtl number Pr, kept identical in both phases, is varied across three representative values – 0.07 (liquid metals), 0.7 (vapour) and 7 (water) – to span thermal transport regimes across three orders of magnitude. The simulations are conducted at a friction Reynolds number $Re_\tau = 150$, void fraction $\alpha = 5.4\,\%$ and a density ratio $\rho_r = 0.1$ (defined as the bubble-to-carrier density). The bubbles substantially alter the hydrodynamic structure of the flow, amplifying turbulent fluctuations and mixing. Their interaction with the thermal boundary layers disrupts the characteristic streaky structures near the heated walls, fragmenting them into smaller and more chaotic patterns. To elucidate this mechanism, we examine the bubble-induced modifications to the temperature field and show that temperature becomes decorrelated from velocity. Consequently, the heat-transfer enhancement arises primarily from an increase in convective heat flux driven by intensified wall-normal velocity fluctuations. The thermal boundary layer is markedly thinned, and the Nusselt number nearly doubles across all examined cases.

Key words: drops and bubbles, turbulent mixing, channel flow

---

1. Introduction

Industrial processes, such as those in chemical and nuclear power plants, often involve the intentional initiation of boiling or the injection of bubbles into a turbulent working fluid. The rationales for introducing a dispersed gaseous phase in practical applications are manifold and depend on the desired process enhancement.

For example, in steel-making operations, gas blowing promotes the circulation and homogenisation of molten steel, while simultaneously enhancing its cleanliness (Wang *et al.* 2020; Yang *et al.* 2020*b*; Chang *et al.* 2021). Impurities can adhere to the bubble surfaces (Zhang & Taniguchi 2000; Yang *et al.* 2020*a*) or become entrained in the bubble wakes (Söder *et al.* 2004; Xu, Ersson & Jönsson 2016; Lou & Zhu 2016), facilitating their removal. However, the presence of small bubbles also poses challenges: they can become trapped in solidifying shells, leading to defects in the final cast material (Yang *et al.* 2020*b*).

Similarly, in biotechnological and pharmaceutical industries, fermentation processes rely on bubble spargers to supply oxygen needed by microorganisms for metabolite production (Gelves, Dietrich & Takors 2014; Niño *et al.* 2023). Successful aeration is dictated by multiple factors, such as bubble size distribution, bubble area distribution, mass transfer coefficient and bubble terminal velocity (Kure, Jakobsen & Solsvik 2024; Hosen *et al.* 2024).

Another important example arises in boiling water reactors, where heat removal enhancement is achieved through boiling processes (Silvi *et al.* 2021; Roccon 2025). Initially, the cooling fluid enters the reactor core as a single-phase liquid and subsequently evaporates due to the heat transferred from the fuel rod walls. The nucleation and growth of bubbles require the absorption of latent heat, thereby extracting thermal energy from the surrounding hot liquid. Following detachment from the heated surfaces, the vacated volume is replenished by colder liquid, promoting local cooling. The detached bubbles then rise through the fluid due to buoyancy forces, enhancing vertical mixing and further contributing to heat removal (Lienhard IV & Lienhard V 2005; Lakkaraju *et al.* 2013).

Despite the diversity of these applications, they share common underlying physical mechanisms: the introduction of a dispersed gaseous phase leads to highly complex flow phenomena (e.g. coalescence and breakage), primarily due to the action of buoyancy forces on the bubbles. Buoyancy not only governs the motion of the dispersed phase but also generates additional shear in the carrier liquid, modifying the local turbulence structure (Bunner & Tryggvason 2003; Lu, Fernández & Tryggvason 2005; Riboux, Risso & Legendre 2010; Ravelet, Colin & Risso 2011; Bolotnov 2013). However, a fundamental understanding of key local phenomena, such as the bubble wake dynamics and trajectory instabilities, remains limited. Historically, the simulation of turbulent multiphase flows was extremely challenging due to the demanding computational cost associated with resolving the wide range of spatial and temporal scales involved. As a result, early research efforts predominantly relied on experimental studies (Serizawa, Kataoka & Michiyoshi 1975; Wang *et al.* 1987; Liu 1993). In recent years, advancements in computational power and numerical methods have enabled the research community to increasingly focus on the detailed simulation of multiphase turbulent flows, providing new insights into previously inaccessible aspects of these systems (Santarelli, Roussel & Fröhlich 2016; Lu & Tryggvason 2018; du Cluzeau, Bois & Toutant 2019; Lu & Tryggvason 2019; du Cluzeau *et al.* 2022; Lee *et al.* 2024; Lu, Yang & Deng 2025). Most of these numerical studies have focused on the modulation of turbulence due to the dispersed phase, particularly in canonical configurations. In contrast, despite their central role in numerous industrial processes, significantly fewer efforts have been devoted to understanding how bubbles influence passive scalar transport or heat transfer.

Among the earliest studies in this direction, Tanaka (2011) investigated heat transfer in a turbulent vertical channel with bubble injection, without accounting for bubble break-up or coalescence. His findings indicated that heat transfer was enhanced relative to both single-phase flows and cases with neutrally buoyant droplets; however, this improvement was accompanied by increased wall-shear stress. These results suggest that the net benefit of bubbly flows for heat transport depends critically on the interplay between buoyancy-induced motion and frictional losses at the wall. Deen & Kuipers (2013) examined the behaviour of a single bubble and a few bubbles rising near a heated wall. They showed that the local heat-transfer coefficient peaks in the vicinity of the bubble due to thinning of the thermal boundary layer. Moreover, bubble-induced agitation significantly enhanced wall–liquid heat transfer, especially in regions where coalescence prevailed. Successively, Dabiri & Tryggvason (2015) analysed heat transfer in a turbulent vertical channel flow laden with bubbles. They focused on the effect of the surface tension in the non-coalescing/breaking case. Their simulations demonstrated that the largest enhancement in heat transfer occurred at a low surface tension value. In particular, nearly spherical bubbles rising close to the walls disrupted the viscous sublayer and reduced the thickness of the conduction-dominated region, thereby increasing the heat-transfer rate. Similarly, Panda *et al.* (2019) investigated the effect of the volume fraction, reporting a plateau in the global heat exchange enhancement. More recently, research has extended to the behaviour of passive scalars in homogeneous bubbly suspensions. Notably, Loisy, Naso & Spelt (2018) explored the convective contributions to effective scalar diffusivity, while Hidman *et al.* (2023) provided physical interpretations of the observed -3 scaling in the scalar energy spectrum.

From the experimental perspective, the seminal work of Deckwer (1980) investigated heat transfer in column bubble reactors, combining the surface renewal model (Kast 1962) with Kolmogorov’s isotropic turbulent theory. Further studies highlighted the connection between the bubble-induced turbulence – composed of the induced liquid motion and the turbulence created in their wakes – and the heat-transfer enhancement both in liquid metals (Tokuhiro & Lykoudis 1994) and water (Kitagawa, Kitada & Hagiwara 2010; Kitagawa & Murai 2013; Kitagawa, Denissenko & Murai 2017). Subsequent works on homogeneous bubbly flows attested the predominance of the bubble-induced mixing over natural convection, modelling the mixing as a diffusion process (Alméras *et al.* 2015; Gvozdić *et al.* 2018). Similarly to Hidman *et al.* (2023), Dung *et al.* (2023) examined the modification of the scalar spectrum of a turbulent flow due to bubble injection. They speculated that the transition from the $-5/3$ to -3 scaling is mainly due to the enhanced homogenisation promoted by the dispersed phase, which reduces the small-scale temperature differences.

Although passive scalar transport has received attention, a comprehensive discussion of the combined effects of shear-induced and bubble-induced turbulence, which includes coalescence and breakage phenomena, on the heat transfer is still lacking. It is worth highlighting that topological changes might lead to very different volume fraction distributions with significant effects on turbulent modulation. In this study, we perform direct numerical simulations (DNS) of turbulent bubbly upflows in a vertical channel using a volume of fluid (VOF) method (Lee *et al.* 2024; Lu *et al.* 2025). Our goal is to investigate how a swarm of large, deformable bubbles alters the heat-transfer process across different thermal transport regimes. Specifically, we choose three different Prandtl numbers $Pr = 0.07$, 0.7 and 7.0 (i.e. ratio of momentum-to-thermal diffusivity) representative of the thermal properties of liquid metals, vapour and water, respectively. To the extent of the authors' knowledge, this is the first attempt to characterise heat-transfer modulation in a heterogeneous bubbly system across three orders of magnitude of Pr, using DNS.

This paper is structured as follows. We begin in § 2 by outlining the governing equations and numerical methods. Section 3 then details the simulation set-up. The results are presented in § 4, where we first examine the qualitative behaviour before delving into the turbulence modifications driven by the bubbles and their effect on temperature statistics and heat transfer. Finally, § 5 provides a summary of the key findings and conclusions.

2. Governing equations

We employ DNS of the Navier–Stokes equations coupled with a VOF method to study the heat-transfer process in a differentially heated bubble-laden turbulent Poiseuille channel flow.

The two immiscible fluids are modelled applying the 'one-fluid' approach (Prosperetti & Tryggvason 2007; Elghobashi 2019), where a single set of continuity, Navier–Stokes and energy equations describes the fluid and temperature dynamics in both phases. Within this framework, the resulting non-dimensional governing equations are

$$\nabla \cdot \boldsymbol{u} = 0, \tag{2.1}$$

$$\rho\left(\frac{\partial \boldsymbol{u}}{\partial t} + \nabla \cdot (\boldsymbol{u}\boldsymbol{u})\right) = -\nabla p - \beta \boldsymbol{i} + \frac{1}{Re_\tau}\nabla \cdot \left(\mu\left(\nabla \boldsymbol{u} + \nabla \boldsymbol{u}^T\right)\right) + \frac{1}{We}\boldsymbol{f}_\sigma - \frac{\rho - \rho_{av}}{Fr}\boldsymbol{i}, \tag{2.2}$$

$$\frac{\partial \theta}{\partial t} + \nabla \cdot (\boldsymbol{u}\theta) = \frac{1}{\rho}\frac{1}{Re_\tau Pr}\nabla \cdot (\kappa \nabla \theta), \tag{2.3}$$

$$\frac{\partial \chi}{\partial t} + \nabla \cdot (\boldsymbol{u}\chi) = 0, \tag{2.4}$$

where $\chi = \chi(\boldsymbol{x}, t)$ is the phase indicator, $\boldsymbol{u} = \boldsymbol{u}(\boldsymbol{x}, t)$ is the fluid velocity, $\rho = \rho(\boldsymbol{x}, t)$ is the local density, ρ_{av} is the average weight of the mixture in the whole channel, $\mu = \mu(\boldsymbol{x}, t)$ is the local dynamic viscosity, $\theta = \theta(\boldsymbol{x}, t)$ is the local temperature, $\kappa = \kappa(\boldsymbol{x}, t)$ is the local thermal conductivity, $\boldsymbol{f}_\sigma$ is the surface tension force and, $\nabla p = \nabla p(\boldsymbol{x}, t)$ is the pressure gradient that drives the flow in the streamwise direction $\boldsymbol{i}$ (oriented upwards). The term $\beta = dP/dx + \rho_{av}/Fr$ is an effective pressure gradient that considers the effect of the mean buoyancy (Lu & Tryggvason 2018, 2019; Cifani, Kuerten & Geurts 2020; Lee *et al.* 2024; Lu *et al.* 2025). This treatment arises from the mean momentum balance, where $\tau_w = h\beta$, with h being the half-channel width, $\tau_w = \tilde{\rho} u_\tau^2$ the wall-shear stress. Note that, henceforth, the symbol $\tilde{\cdot}$ denotes the reference quantities used for non-dimensionalisation. Consequently, imposing β is equivalent to imposing the friction velocity u_τ (absolute value) and direction of the flow (upflow or downflow).

The surface tension force is modelled as a volumetric force (continuum surface force model) concentrated at the interface (Brackbill, Kothe & Zemach 1992)

$$\boldsymbol{f}_\sigma = k\delta_D(\boldsymbol{x} - \boldsymbol{x}_s)\,\boldsymbol{n}, \tag{2.5}$$

where $\boldsymbol{n}$ is the unit normal to the interface, k is the local curvature of the interface between the two fluids and the Dirac function δ_D identifies the interface location $\boldsymbol{x}_s$ (Tryggvason, Scardovelli & Zaleski 2011). In particular, the curvature is computed with a combination of the height function technique (Cummins, Francois & Kothe 2005; Francois *et al.* 2006; Popinet 2009) and least-squares method (Ding *et al.* 2004), which guarantees low spurious currents. A thorough validation of the surface tension can be found in the appendix of Di Giorgio, Pirozzoli & Iafrati (2022), and in Di Giorgio, Pirozzoli & Iafrati (2024).

The presence of a surface tension force in (2.2) ensures that the Laplace pressure jump and velocity slip at the interface are naturally captured (Landau & Lifshitz 1987), thereby making the velocity and stresses continuous across the deformable interface (Tryggvason *et al.* 2011).

Equation (2.3) – also known as the energy equation in the incompressible limit – describes the evolution of the temperature field, which is treated as a passive scalar in the present case. Due to the one-fluid formulation and the continuous definition of thermal conductivity across the interface, temperature is inherently continuous, thus requiring no explicit jump conditions at the interface (Roccon, Zonta & Soldati 2023).

In the present work, the geometric VOF method proposed by Weymouth & Yue (2010) is employed to track the interface, which involves solving (2.4) for the transport of the phase indicator. In VOF, the phase indicator χ represents the volume fraction of one of the two phases (e.g. dispersed phase). The local density, viscosity and thermal conductivity are then defined as

$$\rho = \chi + (1-\chi)\,\frac{\rho_b}{\rho_c}, \quad \mu = \chi + (1-\chi)\,\frac{\mu_b}{\mu_c}, \quad \kappa = \chi + (1-\chi)\,\frac{\kappa_b}{\kappa_c}, \tag{2.6}$$

where subscripts c and b refer to the liquid (carrier) and gas (bubble) phase, respectively.

The dimensionless flow parameters that appear in (2.2)-(2.3) are the shear Reynolds Re_τ (ratio of inertial to viscous forces), Weber We (ratio of inertial to surface tension forces), Froude Fr (ratio of inertial to gravitational forces) and Prandtl Pr (ratio of momentum to thermal diffusivity) numbers, defined as

$$Re_\tau = \frac{\tilde{U}\tilde{L}\tilde{\rho}}{\tilde{\mu}}, \quad We = \frac{\tilde{\rho}\tilde{U}^2\tilde{L}}{\sigma}, \quad Fr = \frac{\tilde{U}^2}{g\tilde{L}}, \quad Pr = \frac{\tilde{\mu}\tilde{c}_p}{\tilde{\kappa}}, \tag{2.7}$$

where σ is the surface tension coefficient and g is the gravitational acceleration. The reference values for density, dynamic viscosity, specific heat capacity, thermal conductivity, length and velocity are $\tilde{\rho} = \rho_c$, $\tilde{\mu} = \mu_c$, $\tilde{c}_p = c_{p,c}$, $\tilde{\kappa} = \kappa_c$, $\tilde{L} = h$ and $\tilde{U} = u_\tau$, respectively.

In the following, the superscript '+' denotes normalisation in wall units (w.u.) based on the friction velocity u_τ, the viscous length scale $\delta_v = \nu_c/u_\tau$ (where $\nu_c = \mu_c/\rho_c$ is the carrier-phase kinematic viscosity) and the friction temperature $\theta_\tau = q_w/(\rho c_{p,c} u_\tau)$. Accordingly, variables without the '+' superscript are reported in outer units – scaled by the half-channel width h, the friction velocity u_τ, and half-temperature difference between the walls $\Delta\theta_w/2$ – unless otherwise specified.

Equations (2.1) and (2.2) are solved using a projection method. In this approach, the momentum equation is first advanced in time, ignoring the pressure gradient to obtain an intermediate velocity field that does not satisfy the continuity equation. A correction step is then implemented, where the pressure gradient is determined by enforcing the continuity equation and subsequently added to the intermediate velocity field to obtain the correct velocity field (Chorin 1968; Orlandi 2012). Note that we solve the resulting Poisson equation iteratively using the HYPRE library (Falgout & Yang 2002). Time integration employs the Adams–Bashforth explicit scheme for convective and the off-diagonal viscous terms, while the implicit Crank–Nicolson scheme is used for the diagonal diffusion terms. A standard second-order finite difference scheme (Tryggvason *et al.* 2011) is implemented for the spatial discretisation of the viscous terms. Instead, the convective terms require a more careful discretisation due to the possible numerical instabilities connected to the gradients at the interface. As demonstrated by Moin & Verzicco (2016),

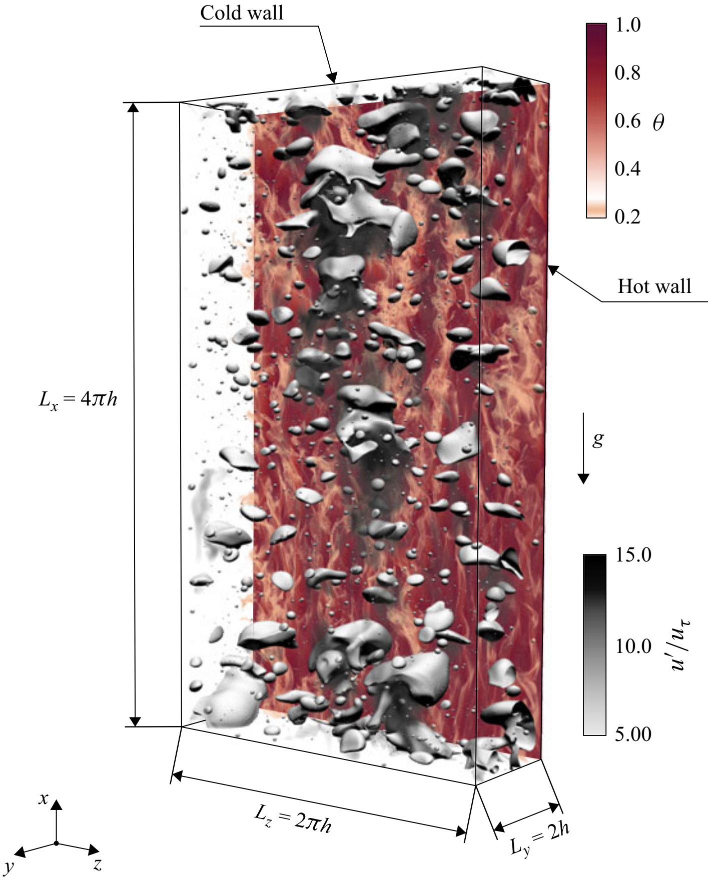

Figure 1. Visualisation of the computational set-up for two immiscible phase flow between heated walls. The flow is driven from bottom to top, with gravity acting in the opposite direction to the flow. White contour surfaces denote the interface separating the two phases. Grey-scale volume rendering illustrates velocity fluctuations u'/u_τ in the carrier phase, specifically highlighting higher positive fluctuations associated with bubble wakes. For clarity, the volume rendering of temperature θ is shown only near the hot wall for the $Pr = 7.0$ case, revealing fine thermal structures bursting from the wall towards the channel centre.

such discretisations on staggered grids provide an optimal balance between accuracy and efficiency for turbulent flow simulations. Therefore, we employ a second-order energy-preserving scheme (Harlow & Welch 1965; Orlandi 2012) in all the regions with uniform χ, and an essentially non-oscillatory scheme at the interface (Shu & Osher 1989). A more in-depth description of the computational method can be found in Di Giorgio *et al.* (2022), Di Giorgio *et al.* (2024) and Rossi, Di Giorgio & Pirozzoli (2025).

3. Simulation set-up

We perform DNS of single-phase and bubble-laden turbulent channel flows (see figure 1) at a fixed friction Reynolds number $Re_\tau = 150$ in a domain of size $4\pi h \times 2h \times 2\pi h$ (streamwise x, wall-normal y and spanwise z directions), driven by a constant effective pressure gradient $\beta = -1$.

The simulations are conducted for three different Prandtl numbers to investigate the influence of thermal conductivity on the flow dynamics. The selected Prandtl numbers span three orders of magnitude, representing different heat-transfer regimes: $Pr_c = 7.0$ for convective liquids (e.g. water), $Pr_c = 0.7$ for diffusive gases (e.g. vapour) and $Pr_c = 0.07$ for highly conductive liquid metals (e.g. NaK). In the bubble-laden cases, we introduce a deformable dispersed phase with bubble-to-carrier density ratio $\rho_r = \rho_b/\rho_c = 0.1$, while keeping matched viscosity ($\mu_c = \mu_b = \mu$) and conductivity ($\kappa_c = \kappa_b = \kappa$). The dynamics is governed by fixed Weber ($We = 0.7$) and Froude ($Fr = 0.014$) numbers. The selection of $\rho_r = 0.1$ is motivated by both numerical and physical considerations. High density ratios present significant challenges for the resolution of the Poisson equation, which becomes computationally demanding as the ratio increases. However, this value is representative of conditions in boiling water reactors operating between 70 and 150 bar, where the density ratio between vapour and water is of the order of 0.1 (Duderstadt & Hamilton 1976; Jain, Tentner & Rizwan-uddin 2009). Regarding the viscosities, the matched dynamic viscosity results in a kinematic viscosity ratio of 10, approximating an air–water system. Furthermore, in buoyancy-dominated regimes, the viscosity ratio has a secondary effect on turbulence modulation compared with the dominant bubble-induced agitation (Lu *et al.* 2025). Finally, the unitary conductivity ratio is chosen to isolate the influence of buoyancy on the heat-transfer process.

Periodicity is imposed in the x and z directions for all variables. At the walls ($y = \pm h$), no-slip conditions are applied to the velocity, no flux to the phase indicator χ and a fixed temperature difference of $\Delta\theta = 2$ ($\theta = \pm 1$ at the walls) is enforced. Initially, we perform a single-phase simulation with a linear temperature profile for each of the Pr values. Once the simulations reach a steady state, we gather statistics for a total of $t^+ = 1500$. These provide both reference baselines and initial conditions for multiphase cases. For the bubble-laden simulations, 256 spherical bubbles of equal size are introduced simultaneously into the fully developed single-phase flow. The bubbles are initialised in two planar structured arrays of 128 bubbles each, centred at the wall-normal positions $y/h = 0.5$ and $y/h = 1.5$. Each bubble has a diameter $d = 0.4h$, corresponding to a global volume fraction $\alpha = 5.4\,\%$. Here, the volume fraction is defined as $\alpha = V_b/(V_b + V_c)$, where V represents the volume of the specific phase. This initial configuration ensures an even distribution across the channel while avoiding unphysical overlaps. Owing to the periodic boundary conditions in the streamwise and spanwise directions, the dispersed phase is naturally conserved. Bubbles or fragments exiting the domain re-enter through the opposite face, thereby maintaining a constant global volume fraction α without requiring artificial reinjection. It is worth highlighting that the bubbles are superimposed on both the velocity and temperature fields, resulting in an initial thermodynamic equilibrium with the surrounding fluid. In order to guarantee that the results are independent of the initial conditions, each case is initialised with a different flow field.

The domain is discretised with $1024 \times 256 \times 512$ grid points in x, y and z, respectively. In viscous units, the resolution is uniform in the homogeneous directions, i.e. $\Delta x^+ = \Delta z^+ = 1.84$. Simultaneously, the wall-normal grid is refined near the walls ($\Delta y^+_{min} = 0.041$) and coarsened towards the centreline ($\Delta y^+_{max} = 1.76$), using the natural grid stretching proposed by Pirozzoli & Orlandi (2021).

This resolution satisfies both the turbulence requirements, by resolving the Kolmogorov scales, η_k, and the thermal Batchelor scales, $\eta_\theta = \eta_k/\sqrt{Pr}$, for all the Pr considered (Batchelor 1971).

An adaptive time-stepping scheme was employed, maintained at a maximum Courant–Friedrichs–Lewy number of 0.25 to ensure numerical stability.

Statistics of the multiphase simulations were collected over $1050\,t^+$, with flow fields sampled every $\Delta t^+ \approx 1.5$. The averaging window was determined by two specific convergence criteria: (i) the stabilisation of the bubble size distribution and (ii) a

Case	Pr_c	Pr_b	Pr_r	Re_τ	We	Fr	$N_x \times N_y \times N_z$	Δx^+	$\Delta y^+_{min,max}$	Δz^+
Single phase	7.0	—	—	150	—	—	$1024 \times 256 \times 512$	1.84	$0.041 - 1.76$	1.84
Single phase	0.7	—	—	150	—	—	$1024 \times 256 \times 512$	1.84	$0.041 - 1.76$	1.84
Single phase	0.07	—	—	150	—	—	$1024 \times 256 \times 512$	1.84	$0.041 - 1.76$	1.84
Bubble laden	7.0	7.0	1.0	150	0.7	0.014	$1024 \times 256 \times 512$	1.84	$0.041 - 1.76$	1.84
Bubble laden	0.7	0.7	1.0	150	0.7	0.014	$1024 \times 256 \times 512$	1.84	$0.041 - 1.76$	1.84
Bubble laden	0.07	0.07	1.0	150	0.7	0.014	$1024 \times 256 \times 512$	1.84	$0.041 - 1.76$	1.84

Table 1. Overview of the main simulation parameters. For fixed Reynolds Re_τ, Weber We and Froude Fr numbers, we consider three Prandtl numbers Pr for both the single-phase and bubble-laden cases. The viscosity ratio is unitary while the density ratio is 0.1. The grid resolution is fixed and sufficiently fine to meet the DNS requirements.

convergence error on the mean Nusselt number (averaged over both walls) below 2 %. This error was calculated following the statistical convergence procedure described in Appendix B in Procacci *et al.* (2025). Mean and fluctuating quantities are obtained by averaging the flow field over the homogeneous streamwise (x) and spanwise (z) directions, followed by temporal averaging over the statistically steady window.

An overview of all simulation parameters is provided in table 1.

4. Results

Before discussing the turbulent statistics and heat-transfer characteristics, it is essential to establish the physical and numerical context of the topological changes observed in this study. A full description of these phenomena would require solving a range of scales spanning from the largest flow scales down to the molecular scales of the interface (Roccon *et al.* 2023). In our VOF framework, bubble breakage and coalescence are handled through the interface-capturing logic, where a colour function implicitly describes the interface position.

There is strong evidence that the Navier–Stokes equations provide a sufficient description of the thread thinning and pinch-off dynamics (Eggers 1995), since these are rapid phenomena dictated by the macroscopic flow physics.

Conversely, bubble coalescence is intrinsically limited by the grid resolution. In real systems, coalescence is governed by the drainage of the liquid film between approaching interfaces – a process that eventually reaches molecular length scales where non-hydrodynamic forces, such as van der Waals interactions, trigger the final rupture. In the present DNS, as in most high-fidelity multiphase studies (Badalassi, Ceniceros & Banerjee 2003; Lu & Tryggvason 2018, 2019; Soligo *et al.* 2019*a*; Cifani *et al.* 2020; Cannon *et al.* 2021; Mangani *et al.* 2022; Bilondi *et al.* 2024; Lee *et al.* 2024; Lu *et al.* 2025), coalescence occurs numerically once the film thickness falls below the grid size. Currently, some numerical methods exploit film drainage models (Kwakkel, Breugem & Boersma 2013), which are based on simplifications such as laminar flow of the film or an imposed interface shape. However, these models might not be fully representative of a real configuration (Allan, Charles & Mason 1961), since the precise physics of liquid film drainage, which governs physical coalescence, remains a debated research topic (Kamp, Villwock & Kraume 2017; Perumanath *et al.* 2019).

With this in mind, we proceed with a qualitative discussion of the results. Then, we present the bubbles' topology and ensure the reliability of the topological representation, validating our results against established theoretical scaling laws, experimental and numerical benchmarks. Successively, we present the turbulent statistics and heat-transfer characteristics.

4.1. *Qualitative results*

A swarm of bubbles is injected into the channel at the beginning of the simulation ($t^+ = 0$), where a turbulent flow is already present. The combined effect of turbulent eddies and buoyancy deforms the interface (Lu & Tryggvason 2018; Soligo *et al.* 2019*b*; Crialesi-Esposito *et al.* 2024; Lu *et al.* 2025), leading to complex liquid–gas interactions. The presence of buoyancy generates a shear velocity between the two phases, which in turn influences the turbulence structures. Under these circumstances, bubbles coalesce and break dynamically throughout the simulation. At first, these interactions are strongly dependent on the initial conditions, but after a transient period, the starting configuration is forgotten. Eventually, coalescence and breakage events balance out, reaching a dynamic steady state where the number of bubbles in the channel remains constant over time. This equilibrium represents a physical balance between the conversion of turbulent kinetic energy into surface energy through fragmentation at large scales, and the reciprocal release of surface energy back into the flow during coalescence at smaller scales (Mukherjee *et al.* 2019; Crialesi-Esposito *et al.* 2022).

Figure 1 provides a visualisation of the complex dynamics within the channel. The white iso-surfaces ($\chi = 0.5$) depict the bubble surfaces, whilst the volume rendering simultaneously illustrates the temperature distribution near the hot wall (red scale) and regions of high velocity fluctuations (grey scale). The combined effect of buoyancy and pressure gradient defines a preferred flow direction. However, both terms induce shear stresses, which in turn affect the bubble distribution in the wall-normal direction. Large, deformable bubbles accumulate at the channel centre, while small, nearly spherical bubbles migrate towards the wall (Lu & Tryggvason 2007; du Cluzeau *et al.* 2020; Lu *et al.* 2025). Notably, the regions of high (positive) velocity fluctuations are primarily located behind the large bubbles (Risso 2016). Conversely, smaller bubbles, characterised by the absence of significant wakes (Mazzitelli, Lohse & Toschi 2003; Ravisankar & Zenit 2024), produce fewer fluctuations. This is because small bubbles generate weak wakes that are attenuated by the interaction with the wall-shear turbulence (Wu & Faeth 1994; Hunt & Eames 2002; Bagchi & Balachandar 2004; Risso 2016).

This turbulent modulation alters the temperature distribution in the carrier. Moreover, the lower density, i.e. lower Re_τ, inside the bubbles affects the relaxation time required by the dispersed phase to adjust to the local temperature. Indeed, the local Péclet number ($Pe = Re_\tau Pr$, defined as the ratio of the advective over the diffusive transport) decreases inside the dispersed phase, where diffusive transport becomes more significant than in the carrier.

Remarkably, the induced agitation of the bubbles affects not only the channel centre (where the bubble wakes are more intense) but also the turbulent structures near the wall. This is noticeable in figure 2, which presents a slice parallel to the wall for each Pr, in both single-phase and multiphase cases, taken at the end of the inner layer ($y^+ = 15$). The background displays the velocity distribution, whilst the iso-temperature contours are colour coded according to the local temperature. Starting with the single-phase cases (figure 2*a*–*c*), the contour lines become closer with increasing Pr, indicating an increase in the local temperature gradients. The dark-red colours for $Pr = 0.07$ confirm that the temperature is relatively uniform with small fluctuations. This is attributed to the characteristic high thermal conductivity of liquid metals, which dissipates the temperature fluctuations at larger scales (Kawamura *et al.* 1998; Na, Papavassiliou & Hanratty 1999;

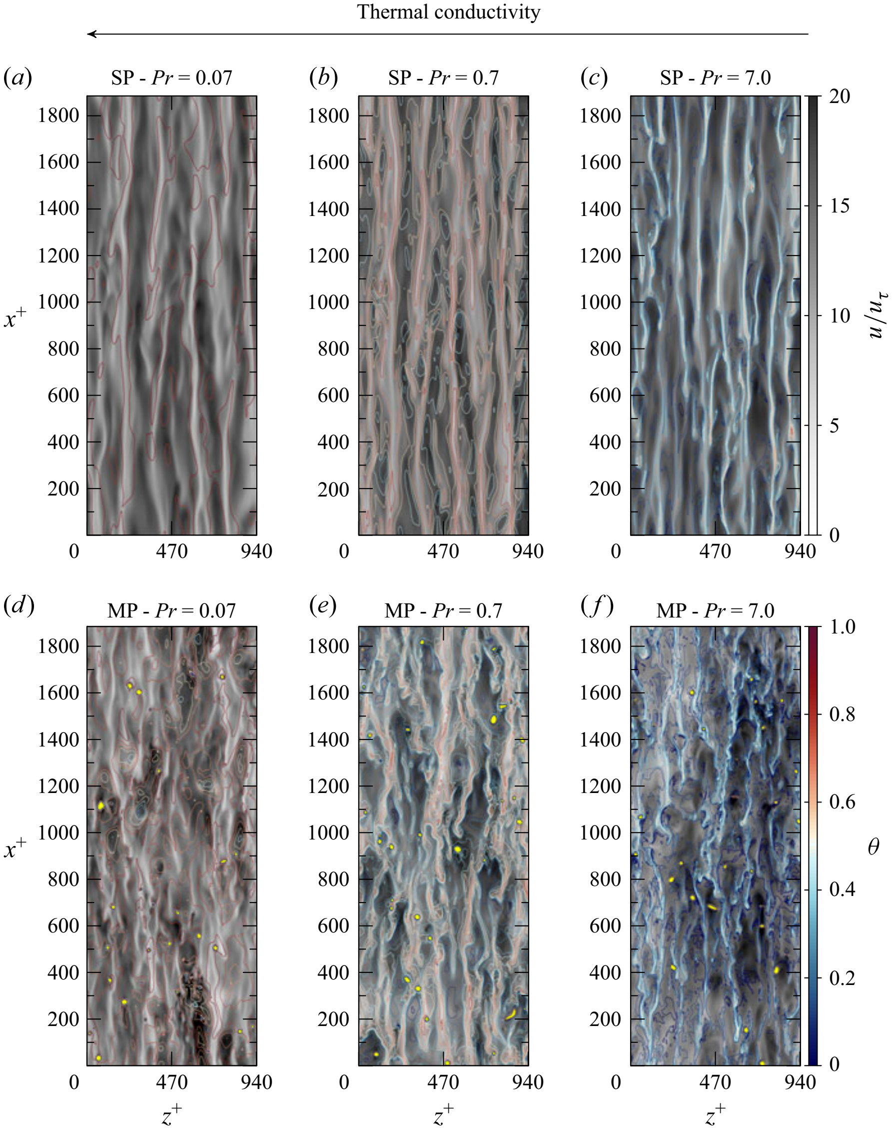

Figure 2. Instantaneous cross-sectional view at $y^+ = 15$ $w.u.$ showing velocity and temperature fields. The top row panels (*a*), (*b*) and (*c*) display the single-phase (SP) cases, and the bottom row panels (*d*), (*e*) and (*f*) present the multiphase (MP) cases. The background represents the velocity field (black for high-velocity regions and white for low-velocity regions). Temperature contours are coloured according to the local temperature (cold: blue, hot: red) and highlight the self-similarity between the velocity and temperature fields for $Pr \gtrsim 1$. In the multiphase case, small bubbles reaching the inner layer are indicated by yellow spots. Observe that the presence of bubbles reduces the streamwise dimension of velocity streaks and enhances mixing.

Piller, Nobile & Hanratty 2002; Procacci *et al.* 2025). As Pr increases, the thermal conductivity decreases, the dissipative scales become smaller, and more intense local gradients are permitted. It is worth noting that for $Pr \gtrsim 1$, the temperature contours follow the Reynolds analogy, showing a good correlation with the velocity streaks in the background. Conversely, the temperature appears decorrelated from the velocity when $Pr \ll 1$.

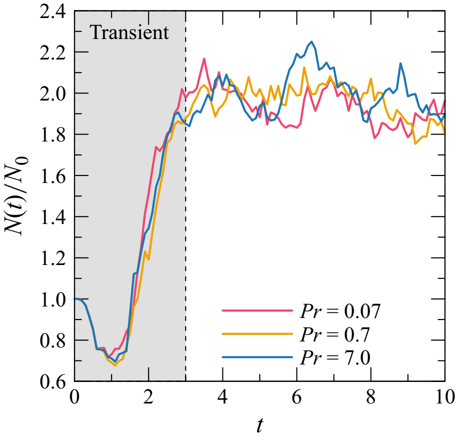

Figure 3. Temporal evolution of the number of bubbles $N(t)$ normalised by the initial value N_0.

In the multiphase cases (figure 2*d–f*), the velocity streaks appear less elongated in the streamwise direction and finer in the spanwise direction. This modification is ascribable to the concurrent action of small spherical bubbles that reach the inner layer (depicted in yellow) together with the agitation introduced in the channel centre by large deformable bubbles. However, the effect of the bubbles is not limited to the velocity streaky structures. Indeed, the temperature contours reveal finer structures in all three cases considered here. In figure 2(*e–f*), the iso-temperature contours exhibit more chaotic patterns with fewer red regions, indicating that colder (warmer) temperatures, characteristic of regions far from the wall, more easily reach the hot (cold) wall. Despite the low Prandtl number (i.e. high conductivity), figure 2(*d*) reveals a larger number of contours compared with the corresponding single-phase case, with a wider colour spectrum, a sign of an increase in thermal structures.

These qualitative observations suggest that bubbles modify the turbulent structures throughout the channel, increasing the mixing. Unlike the single-phase cases, where the temperature field bears a strong resemblance to the underlying velocity field for $Pr \geqslant 1$, the introduction of a dispersed phase leads to a distinct lack of structural similarity between the two fields. This indicates that the Reynolds analogy is not valid in the presence of a dispersed phase.

4.2. *Dispersed-phase topology*

To support these qualitative observations, we begin by analysing the behaviour of the dispersed phase. It is well known that for low volume fractions, such as in the case under scrutiny, reaching the steady-state condition strongly depends on dispersed-phase topology (Lu & Tryggvason 2018, 2019; Lu *et al.* 2025).

Figure 3 shows the evolution in time of the number of bubbles, $N(t)$, normalised by their initial value, N_0. Each Pr is associated with a distinct colour: $Pr = 0.07$ (red-pink), $Pr = 0.7$ (amber) and $Pr = 7.0$ (blue). Despite initialising the simulations with different flow realisations and introducing an initial disturbance to the phase indicator, the bubble's time evolution remains consistent across all cases.

The shear induced by the buoyancy deforms the gas–liquid interface, which in turn opposes a resistance through surface tension. Initially, the surface tension is sufficiently high, leading to a predominance of coalescence events over breakage, which causes the bubbles to merge and form larger bubbles, thereby decreasing the number of bubbles.

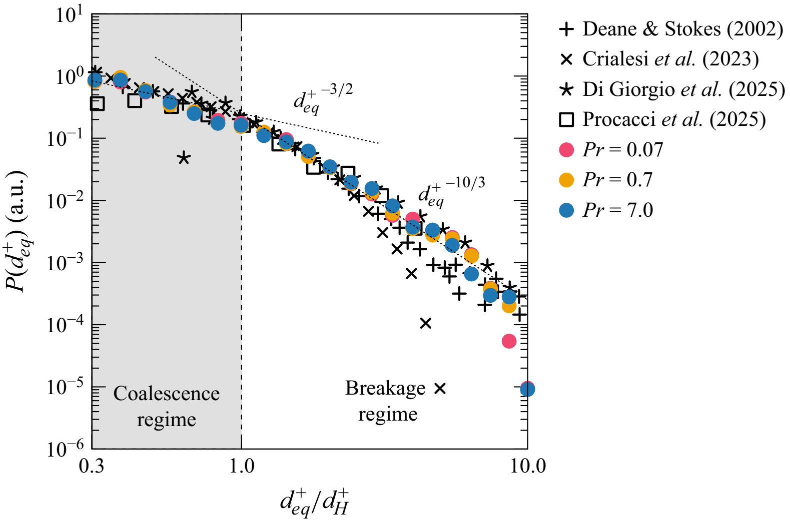

Figure 4. Probability density function, P, of bubbles equivalent diameter, d_{eq}^+, normalised by the Kolmogorov–Hinze scale d_H^+. The plot reveals two distinct regimes: a coalescence-dominated regime following a $-3/2$ scaling law and a breakage-dominated regime exhibiting a $-10/3$ scaling law. A clear transition, marked by a change in slope, is observed at the Hinze scale. For comparative purposes, data from previous studies are shown in black.

However, these larger bubbles are subject to higher accelerations and lower interfacial forces. As a result, at $t = 1$, the breakage events overcome coalescence, leading to an increase in $N(t)/N_0$. Eventually, the surface and buoyancy forces balance out, and a statistical steady state is reached at $t = 3$, where the number of bubbles is approximately twice the initial value.

Once the steady state is reached, the dispersed phase is characterised by a wide range of bubble sizes. A bubble's dimension is commonly represented through its equivalent diameter, d_{eq}^+, defined as the diameter of a sphere with the same volume as the bubble. The population density of bubbles (or droplets) with different d_{eq}^+ is referred to as the bubble size distribution (BSD). Knowledge of the BSD is of paramount importance in multiphase modelling as it contains information about the total interfacial area.

Figure 4 presents the BSD obtained for the different Pr values. The equivalent diameter is normalised by the Kolmogorov–Hinze diameter, d_H^+, which indicates the maximum stable diameter (in w.u.) of a non-breaking bubble (Hinze 1955; Kolmogorov 1991). This scale can be estimated by balancing the external forces contributing to bubble deformation with the stabilising forces. Considering that, in the buoyancy-dominated regime, deformation is primarily driven by the sliding motion between the two phases (Ravelet *et al.* 2011; Ni 2024), the non-dimensional number that best quantifies this force balance is the Eötvös number, $Eo = (\rho_c - \rho_b) g d_H^2/\sigma$. It is reasonable to compute the maximum stable diameter by imposing $Eo = 1$ (Lu *et al.* 2025). Rearranging the definition of Eo with the non-dimensional numbers defined in § 2, we obtain

$$d_H^+ = \left(\frac{\rho_c h^2}{\rho_c - \rho_b} \frac{Fr}{We} Re_\tau^2 \right)^{1/2}, \tag{4.1}$$

where in our case $d_H^+ = 22.36$. This value clearly defines the transition between the coalescence-dominated and the breakage-dominated regimes, characterised by the $-3/2$

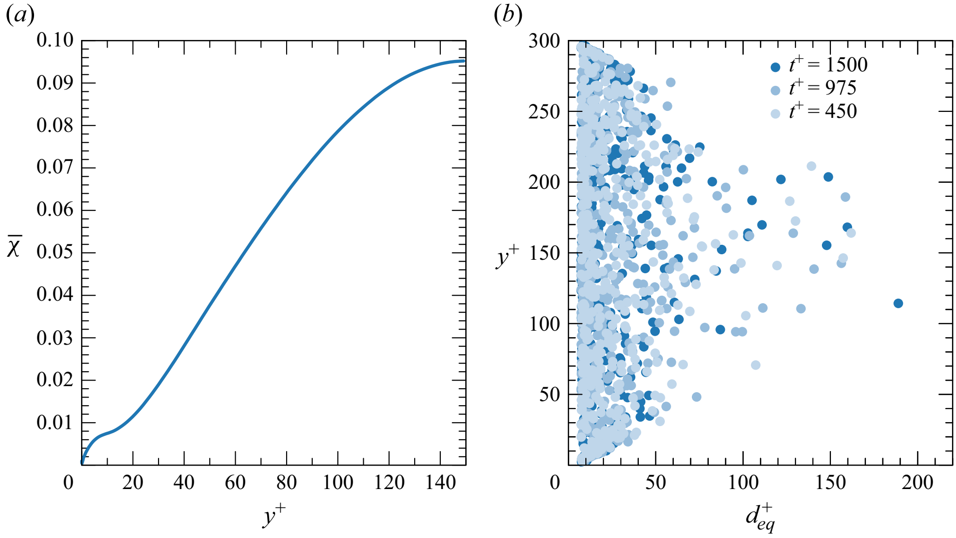

Figure 5. (*a*) Bubble volume fraction, $\overline{\chi}$ and (*b*) scatter plot of the BSDs along the wall-normal direction, y^+. Panel (*b*) shows three different instants: at the beginning of the steady state, half-way and at the end of the simulation.

and $-10/3$ scaling laws, respectively (Garrett, Li & Farmer 2000). In the former regime, bubbles with a diameter smaller than d_H^+ are less likely to break. Conversely, in the latter regime ($d_{eq}^+ > d_H^+$), the surface tension is not sufficient to oppose the external forces, and breakage is most likely to occur. The results are in good agreement with the scaling laws, although the coalescence regime is less wide than the breakage regime due to resolution limitations. It is worth highlighting that the *We* is defined using the half-channel width, as the bubble diameters vary throughout the simulation due to topological changes; this choice is sufficient to capture the relevant breakage and coalescence events.

For comparison, BSDs from different works in the literature are also reported. Specifically, Deane & Stokes (2002) experimentally studied the bubble formation in wave breaking; Crialesi-Esposito, Chibbaro & Brandt (2023) numerically studied the breakage of clean droplets in homogeneous isotropic turbulence; Di Giorgio, Pirozzoli & Iafrati (2025) numerically studied wave breaking; and Procacci *et al.* (2025) numerically studied heat transfer in a channel flow. No sensible difference can be seen in the BSDs across the different cases presented in our study, providing further evidence that the initial conditions are forgotten once the steady state is reached.

Finally, we discuss how the bubbles distribute within the cavity. Figure 5(*a*) presents the mean bubble volume fraction profile, $\overline{\chi}$, in the wall-normal direction, y^+. Additionally, figure 5(*b*) shows the BSD along the wall-normal direction at three representative instants during the steady state: the beginning ($t^+ = 450$), the half-way point ($t^+ = 975$) and the end ($t^+ = 1500$). Since the temperature field is treated as a passive scalar, the flow statistics are independent of the Prandtl number. Therefore, we ensemble average the flow fields to obtain higher quality data (Bolotnov 2013).

Interestingly, small bubbles are scattered throughout the whole channel, while a few large bubbles gather in the channel centre. This spatial segregation can be attributed to the effect of deformability on the lift force: large deformable bubbles experience a weakened or reversed lateral lift that promotes centreline accumulation (Lu & Tryggvason 2018; du Cluzeau *et al.* 2019; Lee *et al.* 2024; Lu *et al.* 2025). Conversely, a Magnus-like effect,

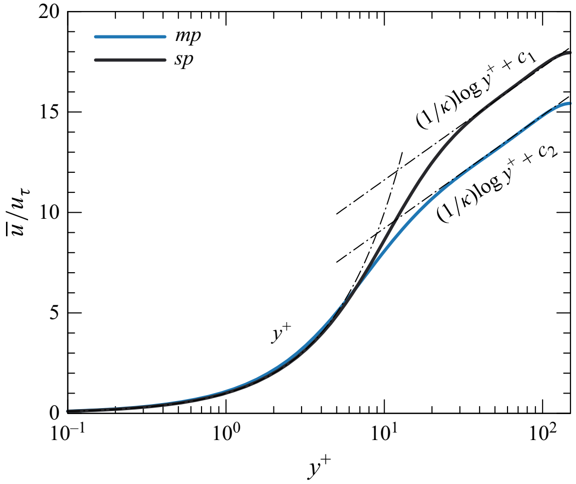

Figure 6. Mean velocity profile along the wall-normal direction in outer units. The dashed–dotted lines show the law of the wall $\overline{u}/u_\tau = y^+$ valid in the viscous sublayer and the log law $\overline{u}/u_\tau = (1/\kappa)\log y^+ + c_i$, with $i = 1, 2$ for the single-phase (sp) and multiphase (mp) case, respectively.

associated with the shear-induced lift force, acts on the small spherical bubbles, forcing them to migrate towards the walls (Lu, Biswas & Tryggvason 2006; du Cluzeau *et al.* 2020). Tomiyama (1998) and Tomiyama *et al.* (2002) attributed the weakening or reversal of the lift force in deformable bubbles to the interaction between their wake and the surrounding shear field. However, this is a dynamic state where small bubbles, forming after a break-up, migrate towards the walls but can coalesce again before actually reaching the wall, or get trapped in the wake of the large bubbles. This competition between migration and coalescence prevents a strict accumulation at the walls. The overall volume fraction exhibits a core-peaking distribution, indicating that the larger bubbles contribute more to the total volume. This spatial segregation of bubble sizes is a key feature of the dispersed-phase topology, directly influencing the local modulation of turbulence and heat transfer.

4.3. *Hydrodynamics*

We now focus on the turbulent characteristics of the bubble-laden flow, prior to discussing temperature and heat transfer. The velocity field, ensemble averaged across the three Prandtl numbers, is analysed.

Figure 6 shows the mean velocity profile $\overline{u}/u_\tau$ of the carrier phase along the wall-normal direction for the multiphase (blue solid line) and the single-phase (black solid line) cases. For comparison, the law of the wall and the log law (dashed–dotted black lines) are also reported. In the viscous sublayer ($y^+ \lesssim 5$), both single-phase and bubble-laden flows follow the linear scaling $\overline{u}/u_\tau = y^+$. In this region of the channel, the effect of the bubbles is negligible, primarily because very few bubbles reach it, and those that do are predominantly small spherical bubbles with a negligible wake. By contrast, the logarithmic region is significantly affected by the bubble motion. The carrier phase reaches a lower velocity peak at the channel centre, which aligns with previous studies (Dabiri, Lu & Tryggvason 2013; Santarelli *et al.* 2016; Lu & Tryggvason 2018, 2019; Lee *et al.* 2021). This reduction is attributed to the core-peaking distribution of $\overline{\chi}$, which impedes the carrier flow. Interestingly, in contrast to the findings reported in Lu *et al.* (2025), who did not observe a logarithmic layer in their multiphase case, we find a more spatially extended

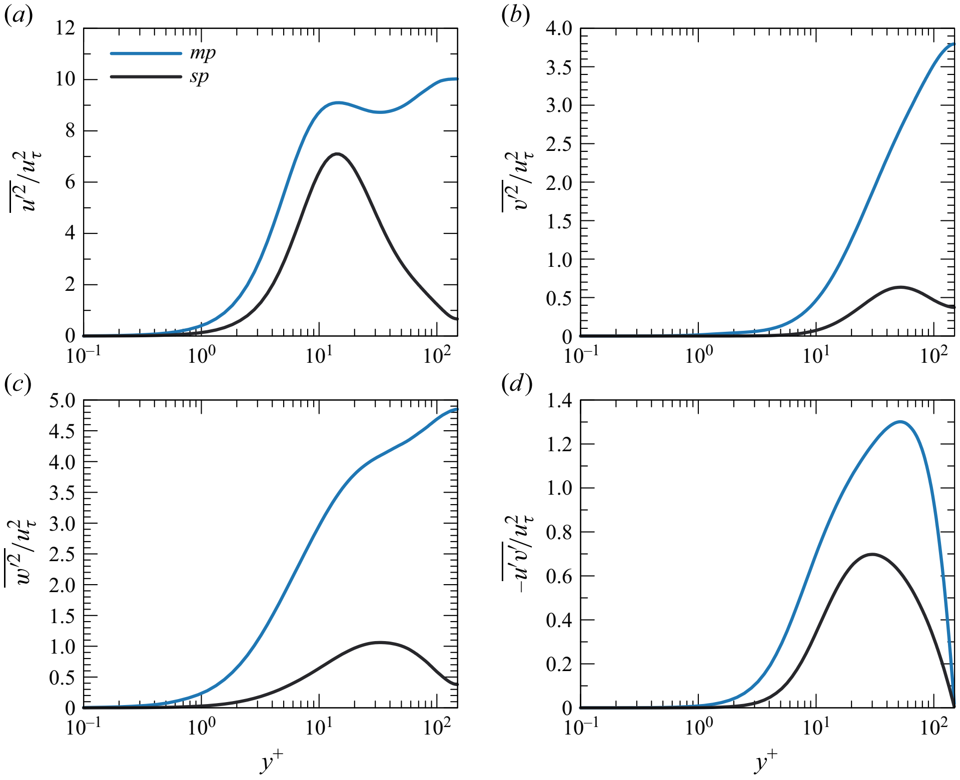

Figure 7. Velocity variance profile along the wall-normal direction in w.u., where *sp* indicates the single-phase case and *mp* the multiphase case.

logarithmic layer in the multiphase flow compared with the single-phase flow, where the logarithmic layer is barely appreciable due to the low Reynolds numbers considered (see Appendix A). The von Kármán constant κ is found to be approximately 0.41 for both single-phase and bubble-laden flow. However, the additive constants differ, with $c_1 \approx 6.0$ for the single-phase flow and $c_2 \approx 3.6$ for the bubble-laden flow. It is important to note that the existence of a von Kármán constant does not imply its universality in bubbly flows. As demonstrated by Bragg *et al.* (2021), bubbly flows may not exhibit a logarithmic layer at all, depending on the characteristics of the dispersed phase.

Figure 7 shows the contributions to the turbulent kinetic energy (panels *a*–*c*) and the shear Reynolds stress (panel *d*), defined as $\overline{u_i'u_j'}$ where $u' = u - \overline{u}$ denotes the fluctuation from the spatio-temporal mean. These quantities are computed in the carrier phase (blue solid line), as a function of the wall-normal direction (y^+) in logarithmic scale. For comparison, the results of the single-phase case (black solid line) are also shown. The interaction of the shear-induced turbulence and the bubble-induced agitation results in an overall increase in the streamwise u' (panel *a*), wall-normal v' (panel *b*) and spanwise w' (panel *c*) fluctuations in the liquid. In particular, the streamwise fluctuations exhibit a double-peak behaviour with a global peak at the channel centre and a local peak closer to the wall. Conversely, the spanwise and wall-normal fluctuations have a single peak at the channel centre. The enhancement of the Reynolds shear stress $-\overline{u'v'}$ can be explained by balancing (2.2). Whilst for the single-phase case, the shear stress only balances the imposed pressure gradient, in a bubble-laden flow, it also balances the local average density fluctuation (Lu & Tryggvason 2007, 2018). This explains the peak position closer

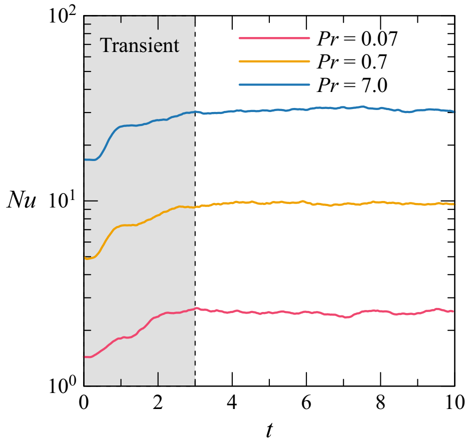

Figure 8. Temporal evolution of the Nusselt number, Nu, averaged over the two walls for the three different Prandtl numbers, Pr.

to the channel centre. It is worth highlighting that the effect of bubble-induced agitation is not restricted to the channel centre; indeed, both normal and shear stresses are enhanced even in the viscous sublayer ($y^+ \lesssim 5$), where the bubbles do not generate strong wakes. Therefore, this higher level of fluctuations can be reasonably attributed to the bubble-induced agitation, especially given that the mean velocity profile exhibits no substantial difference in the gradients near the wall between single-phase and bubbly flows.

Finally, a comparison of the variance values at the channel centre reveals a strong anisotropy. This can be reasonably explained considering that large bubbles, whose wakes are intrinsically anisotropic, are clustered at the channel centre. Procacci *et al.* (2026) showed that this anisotropy is confined to the core region, while in the rest of the channel, the multiphase case shows a greater degree of isotropy than the single-phase case. They associated this energy redistribution with an increase in the sweeps.

4.4. *Temperature*

As discussed, the presence of a buoyant dispersed phase profoundly modifies the turbulence characteristics. Consequently, an alteration of the channel's heat-transfer properties is to be expected. We begin by analysing the temporal evolution of the Nusselt number Nu to ensure that the steady state is reached.

Figure 8 shows the Nusselt number averaged over the two walls, normalised by the respective single-phase value. The Nusselt number is defined as

$$Nu = \frac{2 q_w h}{\kappa_c \Delta\theta}, \tag{4.2}$$

where q_w is the total heat flux at the wall, and $\Delta\theta$ is the temperature difference between the two walls.

The Nusselt number initially increases, followed by a statistical equilibrium. Specifically, the transient period is longer for $Pr = 0.07$ than in the other cases, which corresponds to the time needed for the bubbles to reach a dynamic steady state (as discussed in § 4.2). Although the cases with $Pr = 0.7$ and 7.0 reach the steady state in less time, all statistics were computed from the same temporal instant ($t = 3$) for consistency.

Figure 9(*a*,*c*,*e*) shows the mean scalar distribution in w.u., $\theta^+ = (\overline{\theta} - \theta_w)/\theta_\tau$. Conversely, the temperature is normalised in outer units $\theta^- = (\overline{\theta} - \theta_w)/\Delta\theta$, in

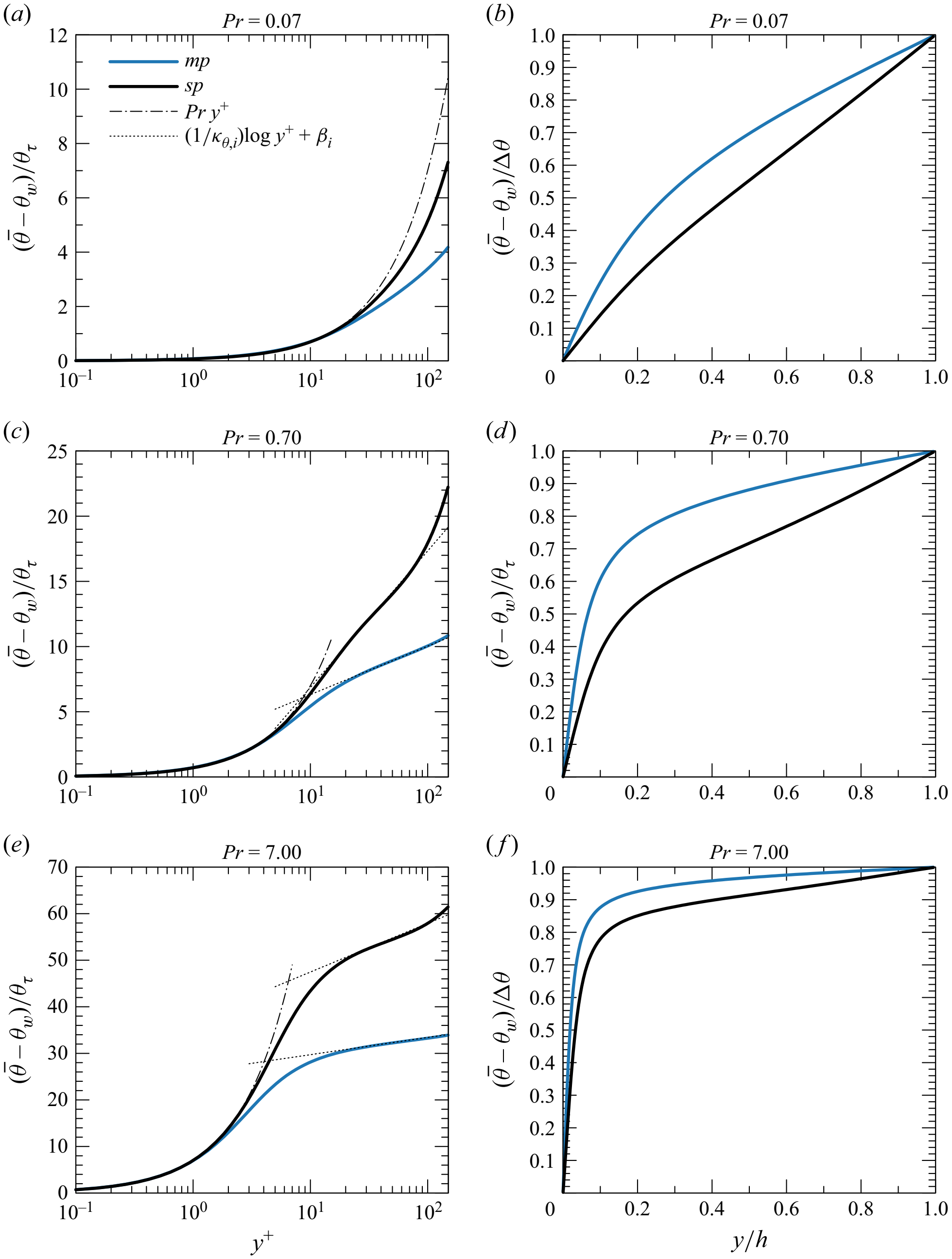

Figure 9. Mean temperature profile in the wall-normal direction scaled by the friction temperature (left column) and the wall-temperature difference (right column). Panels (a),(c) and (e) highlight the thermal sublayer and log layer indicated with a dashed–dotted line. Two different constants for the log layers are identified in the single-phase (sp) and multiphase (mp) cases. The multiphase statistics refer solely to the carrier. Panels (b),(d) and (f) show the higher/lower gradients at the wall/channel centre in the multiphase case.

figure 9(*b*,*d*,*f*). The statistics (reported with a blue solid line) are computed in the carrier phase only. For comparison, the single-phase values are also shown with a solid black line. The black dashed–dotted lines represent the linear conductive sublayer $\theta^+ \approx Pr\ y^+$ (Kader 1981; Kawamura *et al.* 1998; Pirozzoli 2023) and the logarithmic law

$$\theta^+ = \frac{1}{\kappa_{\theta,i}} \log y^+ + \beta_i(Pr), \tag{4.3}$$

where, $\kappa_{\theta,i}$ is the thermal von Kármán constant, where i indicates the single-phase ($i = 1$) or the multiphase case ($i = 2$), and $\beta_i(Pr)$ is the additive constant.

We begin our analysis by examining the single-phase cases, which are essential for understanding the modifications introduced by the bubbles. The inner units representation reveals, for all the considered Pr values, the presence of a conductive layer – the region close to the wall where heat conduction dominates over convection. Specifically, for the low Prandtl number case, no overlap region is observed, as the conductive sublayer penetrates deeply into the velocity logarithmic layer. In contrast, both $Pr = 0.7$ and 7.0 show the presence of a log layer with a thermal von Kármán constant $\kappa_{\theta,1} \approx 0.22$, consistent with the results of Na *et al.* (1999). The additive constant, which is a function of Pr (Kader & Yaglom 1972), has values of approximately −3.6 and 37 for $Pr = 0.7$ and 7.0, respectively. It should also be noted that the mean temperature gradient deviates from the log law at the channel centre, primarily due to the boundary conditions employed in this study (Pirozzoli, Bernardini & Orlandi 2016).

The presence of a gaseous phase modifies the temperature distribution in the carrier phase at $Pr = 0.07$, causing it to deviate from linearity and indicating a more significant role for convection. However, this increase is not sufficiently high to observe an overlap region. An earlier departure from the thermal linear sublayer is also observed at $Pr =$ 0.7 and 7.0. In these cases, the mean temperature is characterised by an extended log layer compared with the single-phase case, where the von Kármán constant $\kappa_{\theta,2}$ is approximately 0.62. This increase in $\kappa_{\theta,2}$ implies a lower gradient and thus a more uniform temperature distribution in the core of the channel. The additive constant $\beta_2(Pr)$ is a function of the Prandtl number, with values of $\beta_2 \approx 2.6$ and 26 at $Pr = 0.7$ and 7.0, respectively. It is important to note that, while the von Kármán constant increases in the multiphase case for both Pr values, the additive constant increases for $Pr = 0.7$ and reduces for $Pr = 7.0$. It is also worth highlighting that the deviation from the log law at the channel centre, which is observed in the single-phase case, is significantly reduced in the bubble-laden case (see Appendix A).

The outer-unit scaling is particularly useful to emphasise the modifications introduced by the bubbles. The temperature at the channel centre is the same in all cases due to the antisymmetric boundary conditions. The single-phase cases clearly show an increase in the temperature gradients at the wall with increasing Pr, while the opposite occurs in the core region.

The bubble-laden cases stress this behaviour. Larger temperature gradients are observed close to the wall, while at the core, the mean temperature appears more uniform. This trend is also valid for the low-Pr case. In the single-phase flow, the temperature gradient is approximately constant throughout the channel. In contrast, the multiphase case shows a clear increase in the gradients close to the wall ($y/h \lesssim 0.3$). This occurs because the bubble wakes, by increasing the velocity fluctuations, allow regions of fluid at different temperatures to come into contact more easily. This suggests that bubbles enhance the temperature mixing by increasing the turbulent fluxes.

The temperature variance is shown in figure 10, where the single-phase statistics (black solid line) are compared with those computed only in the carrier phase (blue solid line).

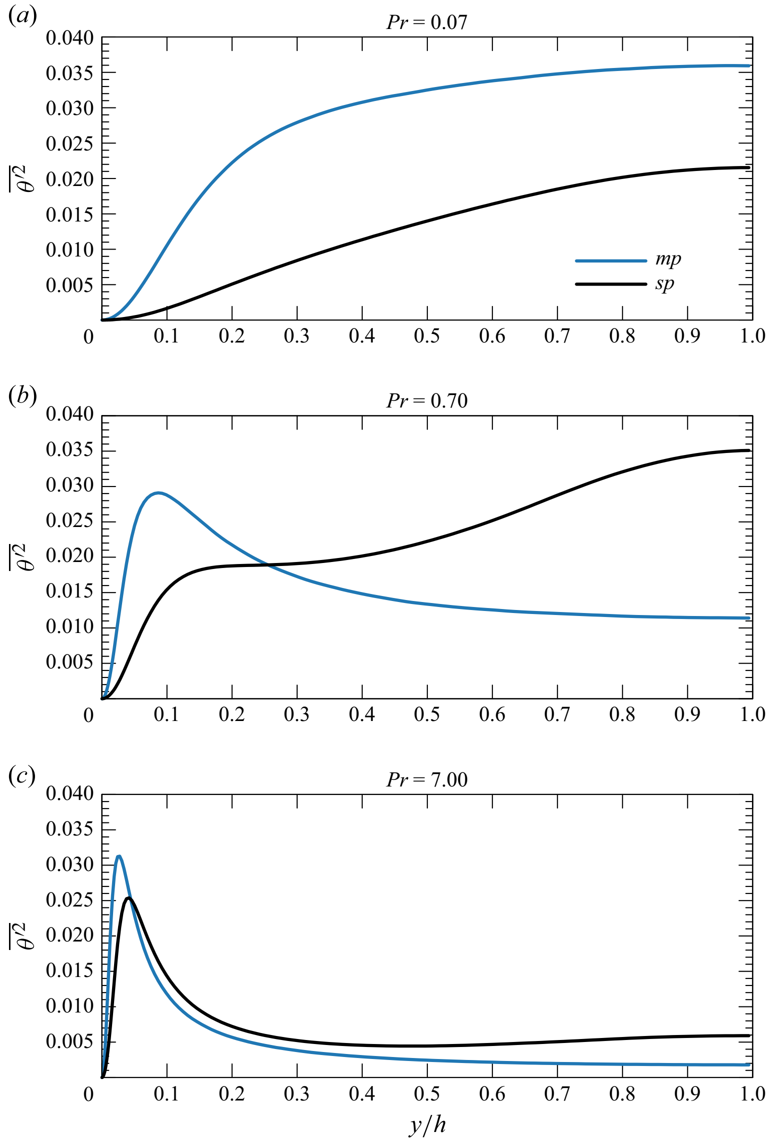

Figure 10. Variance of the temperature in the wall-normal direction for the different *Pr* in outer units. The single-phase (*sp*) cases are used as a reference against the multiphase (*mp*) cases. Notice that the statistics for the multiphase cases refer solely to the carrier phase.

Each panel (*a*,*b*,*c*) refers to a different $Pr = 0.07$, 0.7, 7.0, respectively. Only the outer-scaled profiles are reported here because the friction temperature, which is used for inner-unit normalisation, is a function of the Prandtl number and might be misleading.

At low-*Pr*, the single phase exhibits a lower peak compared with the other cases. This is consistent with the fact that molecular conductivity dominates throughout the entire domain. As a matter of fact, Piller *et al.* (2002) demonstrated, by spectral arguments, that the temperature field loses the ability to respond to large-wavenumber velocity fluctuations with decreasing *Pr*. In other words, dissipation prevails since it occurs in larger eddies (Kawamura *et al.* 1998), thereby reducing temperature fluctuations. Moreover, the variance production, which is related to the mean temperature gradient, is non-zero throughout the

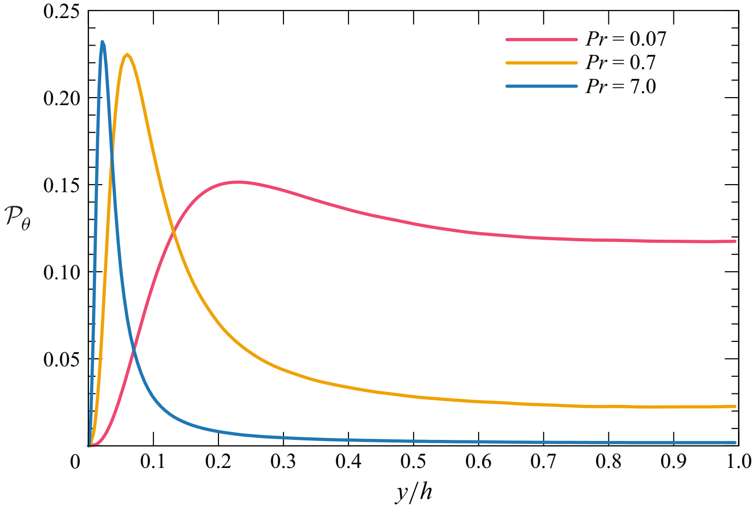

Figure 11. Profiles of the temperature variance production $\mathcal{P}_\theta$ as a function of the wall-normal coordinate y/h for different Prandtl numbers. Statistics are obtained by phase averaging in the carrier phase.

channel (Kasagi, Tomita & Kuroda 1993; Kawamura *et al.* 1998; Na *et al.* 1999), resulting in a core-peaked distribution of the temperature fluctuations (Procacci *et al.* 2025). At $Pr = 0.7$, the temperature variance shows the emergence of a near-wall peak, a feature also present in the streamwise velocity variance profile. However, the similarity cannot be extended to the core region due to the different boundary conditions imposed on u and θ. The enhanced convection at $Pr = 0.7$ leads to more turbulent mixing than at $Pr = 0.07$, but this is not sufficient to eliminate the temperature gradients at the centreline. In contrast, the $Pr = 7.0$ case, which is characterised by an even larger mixing, shows a single maximum of the temperature variance located at the channel centreline. Despite the mean temperature being flatter in the overlap region than in the other cases, a mean temperature gradient is still present, preventing the temperature variance from going to zero.

The presence of bubbles significantly alters the distribution of temperature fluctuation in the channel. At low-Pr (figure 10*a*), the variance profile shows a core-peaked distribution similar to that in the single-phase case, but with a maximum peak that is approximately 1.5 times larger. Furthermore, the fluctuation intensities are larger at every wall-normal coordinate. In particular, $\overline{\theta'^2}$ grows faster than in the single-phase case close to the wall ($y/h \lesssim 3$), where the mean temperature gradients are larger, and then its growth rate reduces. These observations do not apply to $Pr = 0.7$ and 7.0. For $Pr = 0.7$ (figure 10*b*), the scalar variance in the multiphase case exhibits a higher peak in the near-wall region, located closer to the wall than in the single-phase case. In contrast, the fluctuation intensities are less pronounced in the log-law region. Notably, the temperature variance in the carrier phase does not exhibit a peak at the core. This is a consequence of the substantial reduction in the mean temperature gradient, as shown in figure 9(*c*,*d*). Similarly, for $Pr = 7.0$, the fluctuation peak is also enhanced and shifted towards the wall. It is particularly noteworthy that the variance results in a larger value than the single-phase case only up to $y/h \approx 0.04$, which corresponds to the location of the single-phase peak.

The trends in temperature variance observed in figure 10 can be further interpreted by examining the production term $\mathcal{P}_\theta = -\overline{v'\theta'}(\mathrm{d}\overline{\theta}/\mathrm{d}y)$. Figure 11 shows the production profiles, obtained by phase averaging in the carrier phase, for the multiphase cases. The peak production is larger and located closer to the wall for higher Pr, following a similar trend to the temperature variance. For $Pr = 7$ and $Pr = 0.7$, the mean temperature derivative drastically reduces towards the channel centre, and consequently, the production decreases in the core. However, for $Pr = 0.07$, the behaviour differs; despite the departure from the linear trend of the mean temperature, a logarithmic layer is not present. This translates into a non-negligible mean temperature gradient throughout the core, leading to a sustained production term across the channel and explaining the higher variance levels in the core for low Prandtl numbers.

4.5. *Heat fluxes and turbulent transport*

An analysis of the heat-transfer process requires separating the total heat flux into components originating from the carrier and dispersed phases. This decomposition method is similar to approaches used for the total stress balance in rigid spherical particle suspensions (Marchioro, Tanksley & Prosperetti 1999; Zhang & Prosperetti 2010; Picano, Breugem & Brandt 2015) and heat transfer in two-phase flows (Dabiri & Tryggvason 2015; Ardekani *et al.* 2018; Bilondi *et al.* 2024; Procacci *et al.* 2025). Consequently, the total heat flux is given by

$$q''_{tot} = q''_C + q''_D, \tag{4.4}$$

where $q''_C = C_c + C_b$ is the total convective heat flux and $q''_D = D_c + D_b$ is the total diffusive heat flux, resulting from the separate contributions of the carrier and bubbles. Each contribution is computed in dimensionless form as

$$C_c = -\,(1-\overline{\chi})\,\overline{v'_c\theta'_c}, \tag{4.5a}$$

$$C_b = -\overline{\chi}\,\overline{v'_b\theta'_b}, \tag{4.5b}$$

$$D_c = \frac{1}{Re_\tau Pr}\,(1-\overline{\chi})\,\frac{\partial\overline{\theta}_c}{\partial y}, \tag{4.5c}$$

$$D_b = \frac{1}{\rho_r Re_\tau Pr}\overline{\chi}\frac{\partial\overline{\theta}_b}{\partial y}. \tag{4.5d}$$

The density ratio affects the heat transport in two distinct ways. On one hand, its direct influence is local, as it appears only in the diffusion term of the diffusive heat flux in (4.5*d*). On the other hand, its more significant impact is indirect. Working in conjunction with buoyancy, the density ratio modifies the flow's hydrodynamics. This alteration in the flow field subsequently affects heat transport in two ways: it modifies the turbulent heat transfer (convective terms) and also alters the mean temperature distribution (diffusive terms).

Figure 12 depicts the wall-normal profiles of the turbulent $q''_{C,i}$ (in blue) and diffusive $q''_{D,i}$ (in red) heat fluxes normalised by the total heat flux, for each case i considered. The single-phase case is reported in dashed lines, following the same colour coding, as a comparison. At the wall, the constraint imposed on both the velocity and temperature fields allows diffusion to be the only mechanism of transport. Moving further from the wall, the relative importance of the diffusive terms on $q''_{tot,i}$ decreases, and the convective terms become more important. As already reported in previous studies of low Prandtl number (i.e. high conductivity) single-phase flows (Kawamura *et al.* 1998, 1999), convection contributes less to the heat transfer than the diffusion (see figure 12*a*). However, the agitation induced by the bubbles increases both the wall-normal velocity and temperature fluctuations. As a consequence, the convection overcomes the diffusion at $y^+ \approx 35$. Despite the enhancement of the temperature gradients at the wall, $q''_{D,i}$ contributes less

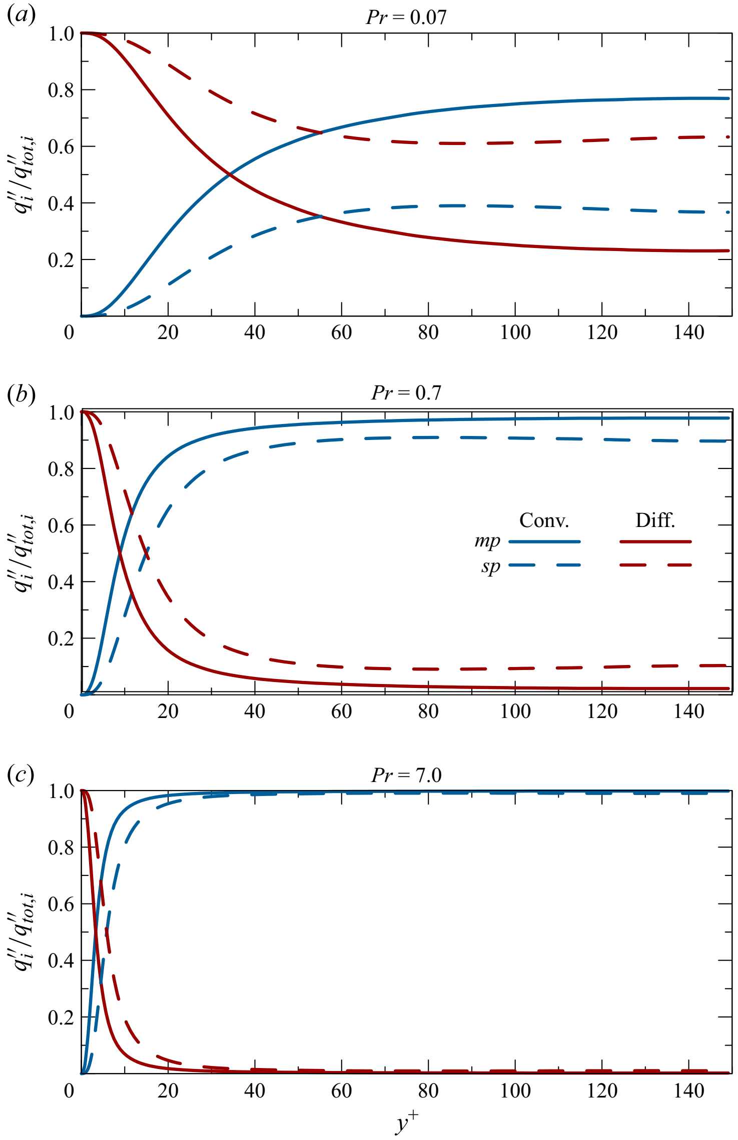

Figure 12. Convective and diffusive heat fluxes for multiphase (mp, solid lines) and single-phase (sp, dashed lines) cases normalised by their total heat flux. Each panel represents a different Prandtl number.

to $q''_{tot,i}$ throughout the whole channel compared with the single-phase case. Nevertheless, the diffusivity accounts for more than 20 % of the heat transfer in the channel centre. This persistence of the diffusive flux in the core region for $Pr = 0.07$ can be interpreted through the filtering effect of molecular thermal diffusivity (Piller *et al.* 2002). In this low-Pr regime, the high thermal conductivity acts as a filter that reduces the effectiveness of high-wavenumber velocity fluctuations – such as the small-scale agitation generated by bubble wakes – in generating scalar fluctuations. This results in a scale separation where the temperature field is primarily influenced by larger-scale structures (Pirozzoli *et al.* 2016). Our results show that, while the bubbles significantly increase the convective contribution

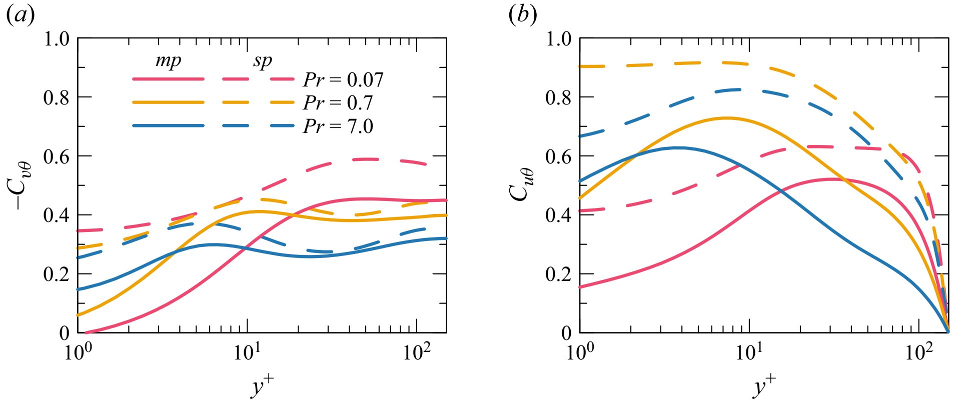

Figure 13. Correlation coefficients between (*a*) wall-normal velocity component and temperature fluctuations, and (*b*) streamwise velocity component and temperature fluctuations. The single-phase (*sp*) cases are used as a reference against the multiphase (*mp*) cases. Notice that *mp* refers to the conditional average in the carrier phase.

(reducing the molecular-to-turbulent diffusivity ratio from approximately 1.7 in the single-phase case to 0.3 in the multiphase case), the molecular diffusion remains a first-order contributor. This prevented homogenisation maintains a non-negligible mean temperature gradient, and thus a significant diffusive flux, across the entire channel. Considering that the Reynolds number is constant, an increase in the Prandtl number corresponds to a rise in the Péclet number, namely, a larger contribution of the advective terms. In fact, the relative importance of the turbulent transport grows faster with increasing Pr, and convection overcomes diffusion at $y^+ \lesssim 20$ (see figure 12*b*,*c*). In contrast to the low-Pr case, in the single-phase case, convection accounts for approximately 90 % of the total heat flux at the channel centre for $Pr = 0.7$ and approximately 99 % for $Pr = 7.0$. The bubbles further increase the turbulent contribution to the total heat flux, restricting the diffusion-dominated region closer to the wall ($y^+ \lesssim 10$). It is interesting to note that the mean temperature gradient at the wall increases regardless of the Pr considered, implying an increase in the diffusive terms that is not observable due to the normalisation. However, this enhancement is not sufficient to oppose the accretion of the turbulent fluxes.

In order to understand the velocity and the temperature fluctuations and their contributions to the turbulent heat fluxes, we introduce the correlation coefficient between two variables a and b

$$C_{ab} = \frac{\overline{a'b'}}{(\overline{a'^2}\;\overline{b'^2})^{1/2}}. \tag{4.6}$$

Figures 13 (*a*) and 13(*b*) show the correlation coefficient for $v-\theta$ and $u-\theta$, respectively. A value of 1 (or -1) indicates that the wall-normal components of the velocity and temperature fluctuations are perfectly correlated (or anticorrelated), while a value close to 0 underlines a decorrelation between the two fields. In line with previous results in the literature (Kasagi *et al.* 1993; Na *et al.* 1999; Piller *et al.* 2002; Pirozzoli *et al.* 2016), $C_{v\theta}$ (in absolute values) is close to 0.3 at the wall and between 0.3 and 0.6 outside the conductive sublayer, in the single-phase case. Despite the convective heat fluxes increasing with Pr, the correlation coefficient results in a decreasing function of Pr. This implies that at larger Pr, the temperature fluctuations contribute more to the heat transfer. Regarding the streamwise correlation, $C_{u\theta}$ reaches high values near the wall for $Pr = 0.7$ and $Pr = 7$, which has been attributed to the fact that flow-oriented vortices control both u' and θ' close to the wall (Kim & Moin 1989; Antonia, Abe & Kawamura 2009). The reduction in $C_{u\theta}$ at $Pr = 7$ is due to the different contribution of the small scales to the fluctuations (Na *et al.* 1999), while the lower correlation at $Pr = 0.07$ results from the higher molecular diffusion rate of the scalar field (Kawamura, Abe & Matsuo 2004). Interestingly, the values of the correlation $u - \theta$ are similar for $Pr \gtrsim 1$ in the outer region, as reported also by (Pirozzoli *et al.* 2016).

The presence of the bubbles reduces the correlation coefficient throughout the whole channel. Specifically, in the near-wall region, the $u - \theta$ correlation values for $Pr = 0.7$ and $Pr = 7$ become nearly identical, while in the outer layer, they increase with decreasing Pr. Notice that now $C_{u\theta}$ values for $Pr = 0.7$ and 7 do not collapse. It is particularly noteworthy that $C_{v\theta}$ reaches a value of 0 at the wall for the low-Pr case, indicating that the two fields are completely decorrelated. Close to the wall, $C_{v\theta}$ increases with Pr, but its growth rate in the channel decreases with Pr. As a result, the correlation coefficient is larger at the channel centre for the low Prandtl number case than for the higher Pr. It is essential to note that only at low-Pr do temperature fluctuations increase, thereby positively contributing to turbulent heat-transport enhancement. In the other cases, the temperature fluctuations decrease as the distance from the wall increases. Therefore, it is reasonable to assume that the enhancement of the heat transfer is mostly because of the higher turbulence induced by the bubble-induced agitation. From a physical point of view, the reduction in $C_{u\theta}$ and $C_{v\theta}$ indicates a decorrelation between the turbulent eddies governing v and θ caused by bubble-induced agitation. The presence of bubbles introduces localised pressure fluctuations, particularly within the wakes (see figure 1). Because the passive scalar field is not directly influenced by these pressure variations, the velocity and temperature fluctuations evolve with different characteristic scales. Consequently, while the bubbles significantly amplify the absolute transport ($\overline{v'\theta'}$), with the velocity playing a more important role, they simultaneously disrupt the statistical coherence of the fluctuations, leading to a breakdown of the Reynolds analogy.

Modelling of the shear stress and convective heat fluxes commonly relies on the Boussinesq hypothesis (Boussinesq 1877), where the turbulent fluxes can be expressed as a gradient diffusion term similar to molecular diffusion, namely

$$-\overline{u'v'} = \nu_t \frac{\partial \overline{u}}{\partial y}, \tag{4.7a}$$

$$-\overline{v'\theta'} = \alpha_t \frac{\partial \overline{\theta}}{\partial y}, \tag{4.7b}$$

where ν_t is the eddy (or turbulent) viscosity and α_t is the eddy (or turbulent) thermal diffusivity. Note that these two quantities are not fluid properties, but depend on the flow conditions. Figure 14 shows α_t and ν_t as functions of the wall-normal distance in w.u. The solid and dashed lines represent α_t in the multiphase and single-phase cases, respectively, with each colour corresponding to a different Prandtl number: $Pr = 0.07$ (red-pink), $Pr = 0.7$ (amber) and $Pr = 7.0$ (blue). The eddy viscosity ν_t is plotted using triangles for the multiphase case, and circles for the single-phase case. Recalling the Reynolds analogy (Reynolds 1874), which suggests that the turbulent-flux terms in the momentum ($\overline{u'v'}$) and energy ($\overline{v'\theta'}$) equations ought to be attributed to the same mechanism, we expect α_t and ν_t to be approximately equal.

In the single-phase cases, the analogy holds for $Pr \gtrsim 0.7$, where negligible variations are observed. In contrast, at $Pr = 0.07$, the turbulent thermal diffusivity is lower than the turbulent viscosity, meaning the Reynolds analogy does not hold at low Prandtl numbers.

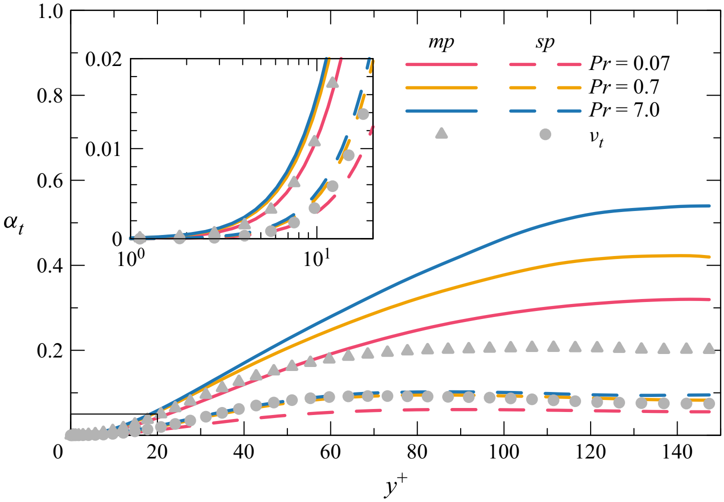

Figure 14. Eddy diffusivity profiles as a function of the wall-normal direction. The solid lines represent the multiphase cases (*mp*), while the dashed lines represent the single-phase case (*sp*). The eddy viscosity is also reported for comparison with triangles and circles for single-phase and multiphase cases, respectively. The inset displays a view of the near-wall region ($y^+ \leqslant 20$) using a semi-log scale.

In the multiphase cases, the similarity between α_t and ν_t is restricted to regions close to the wall. Throughout the rest of the channel, α_t far exceeds ν_t, reaching values of approximately 0.5 in the core. This monotonic increase of the eddy diffusivity away from the wall stems from the competition between the enhanced turbulent heat flux and the flattened mean temperature gradient. While bubble-induced agitation maintains high levels of convective flux $\overline{v'\theta'}$ across the core, the mean temperature gradient $\mathrm{d}\overline{\theta}/\mathrm{d}y$ simultaneously diminishes due to the enhanced mixing. This decoupling of the transport flux from the local mean shear, driven by the local energy injection from bubble wakes, explains the high levels of effective thermal diffusivity.

4.6. *Global heat-transfer coefficients*

Most engineering applications focus on global parameters that simplify complex phenomena, allowing for optimisation of heat transfer characteristics.

One of these parameters is the Nusselt number defined in (4.7*a*), which expresses the relative importance of the convective fluxes over the total heat flux. Figure 15 shows the average (in space and time) value of *Nu* as a function of *Pr*. The empirical prediction of Kays, Crawford & Weigand (1980) is also reported

$$Nu = b_i Pr^{0.5}, \tag{4.8}$$

where $b_1 \approx 10^{0.78}$ and $b_2 \approx 10^{1.04}$ are the corrective coefficients for the single-phase and multiphase cases, respectively. Clearly, *Nu* is an increasing function of *Pr* for both single-phase and bubble-laden cases. Interestingly, the scaling holds in both cases for the entire range of parameters, with a ratio $b_2/b_1 \approx 1.8$. The reasons behind this behaviour might be explained by the Kast (1962) model. They theorised that bubbles force the liquid lateral motion, weakening the boundary layer. Moreover, the wake developed by the bubbles suck the fluid in, promoting a mass exchange with the wall. Deckwer (1980) defined this radial exchange as lateral eddy diffusivity. They also suggested that heterogeneous flows, such as the one under consideration, might not be as effective as homogeneous bubbly flows in

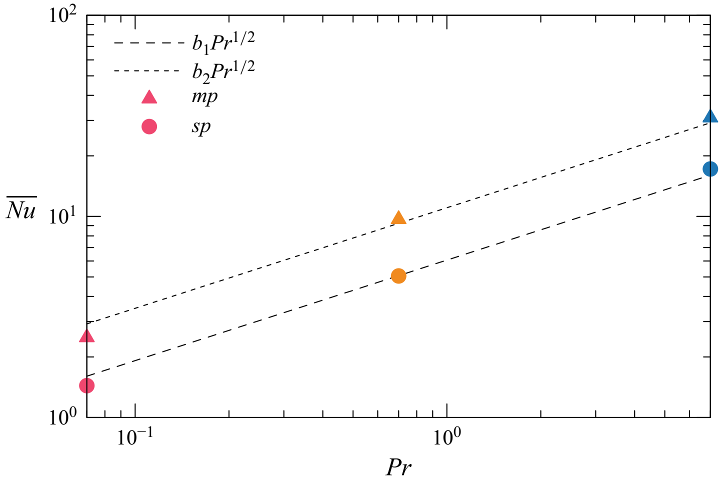

Figure 15. Average Nusselt number $\overline{Nu}$ against the Prandtl number Pr in a log–log scale for single-phase (sp, solid circles) and multiphase (mp, solid triangles) simulations. Both cases follow the same linear trend, with $b_1 \approx 10^{1.04}$ and $b_2 \approx 10^{0.78}$.

improving heat transfer, since large bubbles stir the liquid but do not completely transfer their energy to the micro-scale eddies. Furthermore, the persistence of the $1/2$ scaling in our results suggests that, while the bubbles significantly amplify the magnitude of the turbulent transport, the boundary layer structure remains qualitatively similar to the single-phase case.

Another contribution to heat transfer enhancement is related to the drag increase observed in § 4.3 (Dipprey & Sabersky 1963; Leonardi *et al.* 2015; Orlandi, Sassun & Leonardi 2016; Peeters & Sandham 2019). To quantify this, we consider the Stanton number, St, which expresses the dimensionless heat transfer coefficient

$$St = \frac{\alpha \left. \dfrac{\mathrm{d}\overline{\theta}}{\mathrm{d}y} \right|_w}{u_b(\theta_m - \theta_w)}, \tag{4.9}$$

where α is the molecular thermal diffusivity, θ_b is the mixed (or bulk) mean temperature (Kays *et al.* 1980) and u_b is the bulk velocity. The Stanton number can also be expressed in terms of the Nusselt number

$$Nu = St Re_b Pr, \tag{4.10}$$

where Re_b is the bulk Reynolds number.

The Reynolds analogy relates the friction coefficient C_f to the Stanton number St

$$St \approx \frac{C_f}{2}. \tag{4.11}$$

This relation implies that an increase in C_f directly leads to a proportional increase in St. However, this relation holds only for $Pr \approx 1$. To account for other Prandtl numbers, several corrections have been proposed. For instance, Colburn (1964) experimentally determined a correction

$$St \approx \frac{C_f}{2Pr^{2/3}}. \tag{4.12}$$

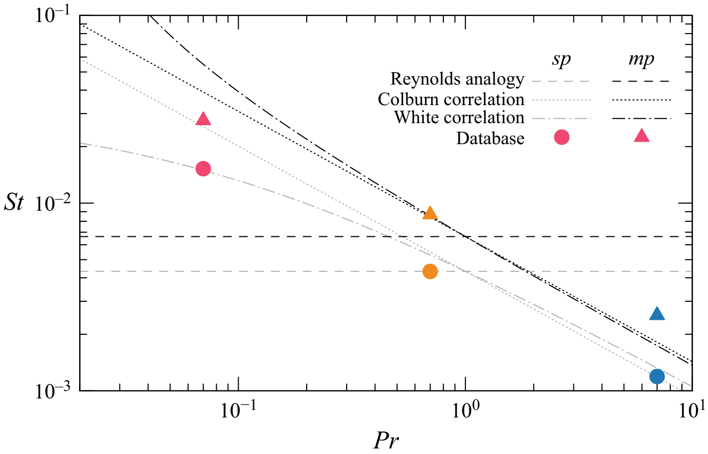

Figure 16. Stanton number St as a function of the Prandtl number Pr in a log–log scale for single-phase (sp, solid circles) and multiphase (mp, solid triangles) simulations. The Reynolds analogy (Reynolds 1874), Colburn correlation (Colburn 1964) and White correlation (White & Majdalani 2006) are reported for comparison purposes, with dashed, dotted and dashed dotted lines, respectively.

A theoretical relation was developed by White & Majdalani (2006) for turbulent flat-plate flows. Their approach involved subtracting the log laws of the velocity and temperature, evaluated at the boundary layer edge, to obtain the following expression:

$$St \approx \frac{C_f/2}{1+13(Pr^{2/3}-1)(C_f/2)^{1/2}}. \tag{4.13}$$

We analysed the validity of these relations in figure 16, which plots St against Pr. Circles represent the single-phase cases, and triangles represent the multiphase cases. The dashed, dotted and dashed–dotted lines correspond to (4.11), (4.12) and (4.13), respectively. The single-phase and multiphase results are distinguished using grey and black lines. Equation (4.11) provides a good prediction only for the single-phase case at $Pr = 0.7$, whereas it underestimates the value at $Pr = 0.07$ and overestimates it at $Pr = 7.0$. Equations (4.12) and (4.13) behave similarly for $Pr \gtrsim 0.7$, but the White correlation is more precise at low Prandtl numbers. None of these relations accurately predicts the Stanton number in the multiphase case, with the single exception of $Pr = 0.7$, where both the Colburn and White correlations provide a good estimate. This was an expected result that further confirms that the bubbles affect the velocity and temperature fields differently. In fact, C_f is approximately 1.5 times larger in the multiphase case compared with the single-phase case, while St increases by 1.8 times. This clearly indicates that the bubbles are more effective at enhancing temperature mixing than at increasing drag.

5. Conclusions

In this work, we performed DNS to investigate the modulation of heat transfer in a turbulent vertical channel flow laden with bubbles. The interface between the two phases was captured using a VOF method, with the energy equation treated as a passive scalar. The simulations were conducted at a fixed shear Reynolds number ($Re_\tau = 150$), Weber number ($We = 0.7$), Froude number ($Fr = 0.014$) and density ratio ($\rho_r = \rho_b/\rho_c = 0.1$). The Prandtl number was varied from 0.07 to 7.0, spanning three orders of magnitude.

We began by characterising the dispersed-phase topology through an analysis of the BSD. After an initial transient ($t^+ \approx 450$), both the total number of bubbles and their size distribution reached a statistically steady state. The Kolmogorov–Hinze scale was found to clearly divide two distinct regimes: a coalescence-dominated regime, which follows a $-3/2$ scaling law, and a breakage-dominated regime, characterised by a $-10/3$ scaling law. Our investigation of the bubble distribution in the wall-normal direction further demonstrated that large bubbles preferentially accumulate in the channel centre, while small bubbles are spread throughout the channel width.

We then compared the one-point statistics of the velocity field averaged in the carrier phase with the single phase. Despite the low Reynolds number, a wider near-logarithmic layer was observed in the bubble-laden case. We also found a reduction of the mean velocity in the channel centre, which aligns with previous reports in the literature (Lu & Tryggvason 2018, 2019; Lee *et al.* 2021; Lu *et al.* 2025). The velocity variances showed an enhancement in all three components, both in the core and close to the wall, even in regions where the dispersed-phase concentration is relatively low.

Our analysis then turned to the temperature statistics. We found that the presence of bubbles induces an earlier departure from linearity in the conductive sublayer for all Pr considered, highlighting the greater influence of convective over diffusive terms close to the wall. We observed no logarithmic layer at low Prandtl numbers. In contrast, the logarithmic layer at $Pr = 0.7$ and 7.0 exhibited a von Kármán constant of 0.62, which is about 2.8 times larger than in the single-phase case, indicating lower gradients, hence larger mixing, in the core region. Interestingly, the additive constant increased at $Pr = 0.7$ and decreased at $Pr = 7.0$. The scalar variance increased only for the low Prandtl number case, while at higher Prandtl numbers, only the near-wall region showed increased activity, with the peak shifting toward the wall. In contrast, the majority of the channel exhibited lower fluctuation values. It is important to note that the temperature fluctuations behave differently from the velocity variance.

The heat flux budget revealed an increased contribution from the turbulent fluxes. It is particularly noteworthy that, for $Pr = 0.07$, the turbulent fluxes overtook the diffusive fluxes at $y^+ \approx 35$. The reduced correlation between the wall-normal velocity and temperature fluctuations suggested that different eddies control v and θ, with those associated with the lateral mass motion playing a more relevant role. Further evidence of the decorrelation between the velocity and temperature fields was obtained by comparing the eddy viscosity with the eddy thermal diffusivity. While these two quantities showed a similar trend in the single-phase case at $Pr = 0.7$, this similarity was completely lost in the multiphase cases.

Finally, we analysed global parameters relevant from an engineering standpoint. The Nusselt number was found to increase with Pr, aligning with empirical laws developed for single-phase flows. Surprisingly, the heat-transfer enhancement in the bubble-laden simulations was independent of Pr, following the same single-phase scaling but with a multiplying constant approximately 1.8 times higher. We also demonstrated that predictions of the heat-transfer coefficient, i.e. St, in the multiphase case, using the correlations widely employed in the single-phase literature, provide satisfactory results only at $Pr = 0.7$.

Overall, the present study was a first attempt to characterise the heat-transfer behaviour of a vertical channel laden with bubbles undergoing complex topological modifications. The Reynolds analogy and other empirical laws were found not to agree with the DNS dataset. Unlike single-phase flows, multiphase simulations are computationally more expensive and involve a greater number of parameters. In fact, the flow is significantly affected by the bubble distribution, which, in turn, depends on the values of Re_τ, Fr, We,

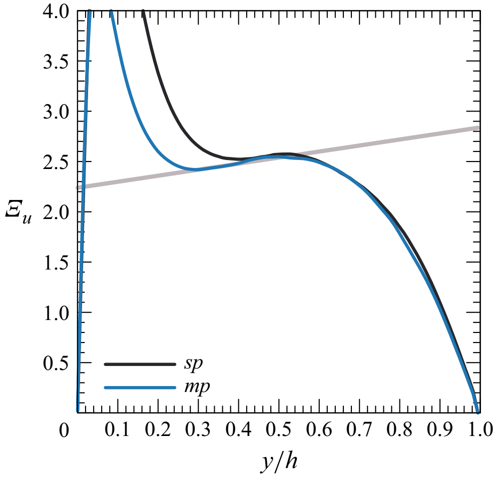

Figure 17. Diagnostic function of the mean velocity for the single-phase simulation (*sp*, black line) and multiphase case phase averaged in the carrier (*mp*, blue line), as defined in (A1). The grey lines correspond to the generalised diagnostic function expressed in (A2).

ρ_r and the volume fraction. Moreover, the thermal response of the system differs with Pr. Ultimately, the development of reliable correlations for these complex multiphase flows will require a more comprehensive investigation spanning a wider range of parameters.

Acknowledgements. We acknowledge EuroHPC for awarding us access to Leonardo (Project ID: R0387) and Sigma2 for awarding us access to Betzy (Project ID: NN9646K). The authors acknowledge NTNU for financial support through its Open Access Funding Program.

Funding. D.P. and J.S. gratefully acknowledge financial support from NTNU.

Declaration of interests. The authors report no conflicts of interest.

Data availability statement. Data are available on request from the authors.

Appendix A. Diagnostic functions

The logarithmic law of the wall arises from the matching condition in a multiscale asymptotic analysis (Pope 2000), where the inner and outer scales are defined by the viscous length ν/u_τ and the channel half-width h, respectively. As the leading-order term in this expansion, the law is formally recovered only in the limit of infinite Re_τ (Jiménez & Moser 2007). To assess its validity at finite Reynolds numbers, we define the logarithmic diagnostic function for both the mean velocity and the passive scalar

$$\Xi_i = y^+ \frac{\mathrm{d}\overline{u}^+}{\mathrm{d}y^+}, \tag{A1}$$

where $i = u, \theta$. A constant value of Ξ_i would imply the presence of a genuine logarithmic layer. To account for the finite Reynolds number effects in our simulations, we adopt the asymptotic analysis of Afzal & Yajnik (1973), which includes a linear term to represent the overlap region at finite Re_τ. The generalised diagnostic function formulation is thus

$$\Xi_i = \frac{1}{\kappa_i} + \alpha_i y + \frac{\beta_i}{Re_\tau}. \tag{A2}$$

Figure 17 illustrates the velocity diagnostic function for the single-phase (black) and carrier-phase (blue) cases as a function of the wall-normal coordinate in outer units. While

i	κ_i	α_i	β_i
u	0.41	0.60	−30
θ_{sp}	0.22	5.20	−2.26
θ_{mp}	0.62	0.40	0

Table 2. Parameters of the diagnostic function defined in (A1) for the velocity u, temperature in the single-phase case θ_{sp}, and temperature in the multiphase case θ_{mp}.

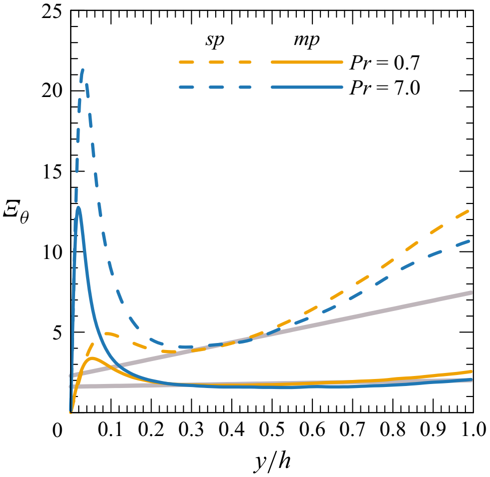

Figure 18. Diagnostic function of the scalar field for the single-phase simulations (*sp*, dashed lines) and multiphase case phase averaged in the carrier (*mp*, solid line), as defined in (A1). The grey lines correspond to the generalised diagnostic function expressed in (A2).

the linear trend, characteristic of the log layer, is relatively short in the single-phase case, the multiphase case clearly exhibits an extended range consistent with the generalised log layer.

Similarly, figure 18 shows the diagnostic function for the passive scalar at $Pr = 0.7$ and 7.0. In the single-phase case, the logarithmic region is narrow, although slightly broader than that of the velocity field. Notably, the shear and agitation introduced by the buoyancy-driven bubbles significantly enhance turbulent fluctuations, promoting a more robust logarithmic behaviour in the thermal statistics compared with the single-phase case.

Values of the coefficients κ_i, α_i and β_i are reported in table 2. The von Kármán constant κ_u of the velocity field matches for both single-phase and multiphase simulations. However, as already specified in § 4.3, there is no indication of universality in bubbly flows. This is supported by the work of Bragg *et al.* (2021) and in Procacci *et al.* (2026); in the latter, the authors investigated different *We*, demonstrating a clear change in the slope of the logarithmic law.

Regarding the mean temperature, the logarithmic layer undergoes a profound modification, with the von Kármán constant κ_θ increasing by approximately a factor of three. Moreover, the linear correction α_θ is notably small in the multiphase case, resulting in an almost genuine logarithmic profile. While this might suggest that the influence of the Reynolds number on the log layer is diminished by bubble-induced agitation, we must clarify that this remains a speculation based on the current data. Indeed, we expect κ_θ to vary with both Re_τ and *We*, as the underlying hydrodynamics and the resulting mixing scales are completely modified by the presence and deformability of the bubbles.

REFERENCES

AFZAL, N. & YAJNIK, K. 1973 Analysis of turbulent pipe and channel flows at moderately large Reynolds number. *J. Fluid Mech.* **61** (1), 23–31.

ALLAN, R.S., CHARLES, G.E. & MASON, S.G. 1961 The approach of gas bubbles to a gas/liquid interface. *J. Colloid Sci.* **16** (2), 150–165.

ALMÉRAS, E., RISSO, F., ROIG, V., CAZIN, S., PLAIS, C. & AUGIER, F. 2015 Mixing by bubble-induced turbulence. *J. Fluid Mech.* **776**, 458–474.

ANTONIA, R.A., ABE, H. & KAWAMURA, H. 2009 Analogy between velocity and scalar fields in a turbulent channel flow. *J. Fluid Mech.* **628**, 241–268.

ARDEKANI, M.N., ABOUALI, O., PICANO, F. & BRANDT, L. 2018 Heat transfer in laminar Couette flow laden with rigid spherical particles. *J. Fluid Mech.* **834**, 308–334.

BADALASSI, V.E., CENICEROS, H.D. & BANERJEE, S. 2003 Computation of multiphase systems with phase field models. *J. Comput. Phys.* **190** (2), 371–397.

BAGCHI, P. & BALACHANDAR, S. 2004 Response of the wake of an isolated particle to an isotropic turbulent flow. *J. Fluid Mech.* **518**, 95–123.

BATCHELOR, G.K. 1971 Small-scale variation of convected quantities like temperature in turbulent fluid. Part 1. General discussion and the case of small conductivity. *J. Fluid Mech.* **5**, 113–133.

BILONDI, A.M., SCAPIN, N., BRANDT, L. & MIRBOD, P. 2024 Turbulent convection in emulsions: the Rayleigh-Bénard configuration. *J. Fluid Mech.* **999**, A4.

BOLOTNOV, I.A. 2013 Influence of bubbles on the turbulence anisotropy. *J. Fluids Engng* **135** (5), 051301.

BOUSSINESQ, J. 1877 Essai sur la théorie des eaux courantes. Impr. nationale.

BRACKBILL, J.U., KOTHE, D.B. & ZEMACH, C. 1992 A continuum method for modeling surface tension. *J. Comput. Phys.* **100** (2), 335–354.

BRAGG, A.D., LIAO, Y., FRÖHLICH, J. & MA, T. 2021 Assessment of the validity of a log-law for wall-bounded turbulent bubbly flows. *Intl J. Heat Fluid Flow* **91**, 108857.

BUNNER, B. & TRYGGVASON, G. 2003 Effect of bubble deformation on the properties of bubbly flows. *J. Fluid Mech.* **495**, 77–118.

CANNON, I., IZBASSAROV, D., TAMMISOLA, O., BRANDT, L. & ROSTI, M.E. 2021 The effect of droplet coalescence on drag in turbulent channel flows. *Phys. Fluids* **33** (8), 085112.

CHANG, S., ZOU, Z., LIU, J., ISAC, M., CAO, X.E., SU, X. & GUTHRIE, R.I.L. 2021 Study on the slag-metal interfacial behavior under the impact of bubbles in different sizes. *Powder Technol.* **387**, 125–135.

CHORIN, A.J. 1968 Numerical solution of the Navier–Stokes equations. *Math. Comput.* **22** (104), 745–762.

CIFANI, P., KUERTEN, J.G.M. & GEURTS, B.J. 2020 Flow and bubble statistics of turbulent bubble-laden downflow channel. *Intl J. Multiphase Flow* **126**, 103244.

DU CLUZEAU, A., BOIS, G., LEONI, N. & TOUTANT, A. 2022 Analysis and modeling of bubble-induced agitation from direct numerical simulation of homogeneous bubbly flows. *Phys. Rev. Fluids* **7**, 044604.

DU CLUZEAU, A., BOIS, G. & TOUTANT, A. 2019 Analysis and modelling of Reynolds stresses in turbulent bubbly up-flows from direct numerical simulations. *J. Fluid Mech.* **866**, 132–168.

DU CLUZEAU, A., BOIS, G., TOUTANT, A. & MARTINEZ, J.-M. 2020 On bubble forces in turbulent channel flows from direct numerical simulations. *J. Fluid Mech.* **882**, A27.

COLBURN, A.P. 1964 A method of correlating forced convection heat-transfer data and a comparison with fluid friction. *Intl J. Heat Mass Transfer* **7** (12), 1359–1384.

CRIALESI-ESPOSITO, M., BOFFETTA, G., BRANDT, L., CHIBBARO, S. & MUSACCHIO, S. 2024 How small droplets form in turbulent multiphase flows. *Phys. Rev. Fluids* **9**, L072301.

CRIALESI-ESPOSITO, M., CHIBBARO, S. & BRANDT, L. 2023 The interaction of droplet dynamics and turbulence cascade. *Commun. Phys.* **6** (1), 5.

CRIALESI-ESPOSITO, M., ROSTI, M.E., CHIBBARO, S. & BRANDT, L. 2022 Modulation of homogeneous and isotropic turbulence in emulsions. *J. Fluid Mech.* **940**, A19.

CUMMINS, S.J., FRANCOIS, M.M. & KOTHE, D.B. 2005 Estimating curvature from volume fractions. *Comput. Struct.* **83** (6–7), 425–434.

DABIRI, S., LU, J. & TRYGGVASON, G. 2013 Transition between regimes of a vertical channel bubbly upflow due to bubble deformability. *Phys. Fluids* **25** (10), 102110.

DABIRI, S. & TRYGGVASON, G. 2015 Heat transfer in turbulent bubbly flow in vertical channels. *Chem. Engng Sci.* **122**, 106–113.

DEANE, G. & STOKES, M. 2002 Scale dependence of bubble creation mechanisms in breaking waves. *Nature* **418**, 839–844.

DECKWER, W.-D. 1980 On the mechanism of heat transfer in bubble column reactors. *Chem. Engng Sci.* **35** (6), 1341–1346.

DEEN, N.G. & KUIPERS, J.A.M. 2013 Direct numerical simulation of wall-to-liquid heat transfer in dispersed gas–liquid two-phase flow using a volume of fluid approach. *Chem. Engng Sci.* **102**, 268–282.

DI GIORGIO, S., PIROZZOLI, S. & IAFRATI, A. 2022 On coherent vortical structures in wave breaking. *J. Fluid Mech.* **947**, A44.

DI GIORGIO, S., PIROZZOLI, S. & IAFRATI, A. 2024 Evaluation of advection schemes and surface tension model for algebraic and geometric VOF multiphase flow solvers. *J. Comput. Phys.* **499**, 112717.

DI GIORGIO, S., PIROZZOLI, S. & IAFRATI, A. 2025 Air entrainment and gas transfer in wave breaking events. *Geophys. Res. Lett.* **52** (15), e2025GL114907.

DING, H., SHU, C., YEO, K.S. & XU, D. 2004 Development of least-square-based two-dimensional finite-difference schemes and their application to simulate natural convection in a cavity. *Comput. Fluids* **33** (1), 137–154.

DIPPREY, D.F. & SABERSKY, R.H. 1963 Heat and momentum transfer in smooth and rough tubes at various Prandtl numbers. *Intl J. Heat Mass Transfer* **6** (5), 329–353.

DUDERSTADT, J.J. & HAMILTON, L.J. 1976 *Nuclear Reactor Analysis*. John Wiley & Sons, Inc.

DUNG, O.-Y., WAASDORP, P., SUN, C., LOHSE, D. & HUISMAN, S.G. 2023 The emergence of bubble-induced scaling in thermal spectra in turbulence. *J. Fluid Mech.* **958**, A5.

EGGERS, J. 1995 Theory of drop formation. *Phys. Fluids* **7** (5), 941–953.

ELGHOBASHI, S. 2019 Direct numerical simulation of turbulent flows laden with droplets or bubbles. *Annu. Rev. Fluid Mech.* **51**, 217–244.

FALGOUT, R.D. & YANG, U.M. 2002 Hypre: a library of high performance preconditioners. In *Computational Science – ICCS 2002* (ed. P.M.A. Sloot, A.G. Hoekstra, C.J.K. Tan & J.J. Dongarra), pp. 632–641. Springer Berlin Heidelberg.

FRANCOIS, M.M., CUMMINS, S.J., DENDY, E.D., KOTHE, D.B., SICILIAN, J.M. & WILLIAMS, M.W. 2006 A balanced-force algorithm for continuous and sharp interfacial surface tension models within a volume tracking framework. *J. Comput. Phys.* **213** (1), 141–173.

GARRETT, C., LI, M. & FARMER, D. 2000 The connection between bubble size spectra and energy dissipation rates in the upper ocean. *J. Phys. Oceanogr.* **30** (9), 2163–2171.

GELVES, R., DIETRICH, A. & TAKORS, R. 2014 Modeling of gas–liquid mass transfer in a stirred tank bioreactor agitated by a rushton turbine or a new pitched blade impeller. *Bioprocess Biosyst. Engng* **37**, 365–375.

GVOZDIĆ, B., ALMÉRAS, E., MATHAI, V., ZHU, X., VAN GILS, D.P.M., VERZICCO, R., HUISMAN, S.G., SUN, C. & LOHSE, D. 2018 Experimental investigation of heat transport in homogeneous bubbly flow. *J. Fluid Mech.* **845**, 226–244.

HARLOW, F.H. & WELCH, J.E. 1965 Numerical calculation of time-dependent viscous incompressible flow of fluid with free surface. *Phys. Fluids* **8** (12), 2182–2189.

HIDMAN, N., STRÖM, H., SASIC, S. & SARDINA, G. 2023 Assessing passive scalar dynamics in bubble-induced turbulence using direct numerical simulations. *J. Fluid Mech.* **962**, A32.

HINZE, J.O. 1955 Fundamentals of the hydrodynamic mechanism of splitting in dispersion processes. *AIChE J.* **1** (3), 289–295.

HOSEN, H.F., SHAHMARDI, A., BRANDT, L. & SOLSVIK, J. 2024 Dynamics of a single bubble in Newtonian and non-Newtonian fluids: experimental and simulation approaches. *Intl J. Multiphase Flow* **174**, 104789.

HUNT, J.C.R. & EAMES, I. 2002 The disappearance of laminar and turbulent wakes in complex flows. *J. Fluid Mech.* **457**, 111–132.

JAIN, P.K., TENTNER, A. & Rizwan-uddin 2009 A lattice Boltzmann framework to simulate boiling water reactor core hydrodynamics. *Comput. Math. Appl.* **58**, 975–986.

JIMÉNEZ, J. & MOSER, R.D. 2007 What are we learning from simulating wall turbulence? *Phil. Trans. A Math. Phys. Engng Sci.* **365**(,1852), 715–732.

KADER, B.A. 1981 Temperature and concentration profiles in fully turbulent boundary layers. *Intl J. Heat Mass Transfer* **24** (9), 1541–1544.

KADER, B.A. & YAGLOM, A.M. 1972 Heat and mass transfer laws for fully turbulent wall flows. *Intl J. Heat Mass Transfer* **15** (12), 2329–2351.

KAMP, J., VILLWOCK, J. & KRAUME, M. 2017 Drop coalescence in technical liquid/liquid applications: a review on experimental techniques and modeling approaches. *Rev. Chem. Engng* **33** (1), 1–47.

KASAGI, N., TOMITA, Y. & KURODA, A. 1993 Direct numerical simulation of passive scalar field in a turbulent channel flow. *J. Heat Transfer* **114** (3), 598–606.

KAST, W. 1962 Analyse des wärmeübergangs in blasensäulen. *Intl J. Heat Mass Transfer* **5** (3), 329–336.

KAWAMURA, H., ABE, H. & MATSUO, Y. 1999 DNS of turbulent heat transfer in channel flow with respect to Reynolds and Prandtl number effects. *Intl J. Heat Fluid Flow* **20** (3), 196–207.

KAWAMURA, H., ABE, H. & MATSUO, Y. 2004 Very large-scale structures observed in DNS of turbulent channel flow with passive scalar transport. In *15th Australasian Fluid Mechanics Conference*, pp. 15–32. The University of Sydney.

KAWAMURA, H., OHSAKA, K., ABE, H. & YAMAMOTO, K. 1998 DNS of turbulent heat transfer in channel flow with low to medium–high Prandtl number fluid. *Intl J. Heat Fluid Flow* **19** (5), 482–491.

KAYS, W.M., CRAWFORD, M.E. & WEIGAND, B. 1980 *Convective Heat and Mass Transfer*. McGraw-Hill.

KIM, J. & MOIN, P. 1989 Transport of passive scalars in a turbulent channel flow. In *Turbulent Shear Flows 6* (ed. J.C. André, J. Cousteix, F. Durst, B.E. Launder, F.W Schmidt & J.H. Whitelaw), pp. 85–96. Springer Berlin Heidelberg.

KITAGAWA, A., DENISSENKO, P. & MURAI, Y. 2017 Effect of heated wall inclination on natural convection heat transfer in water with near-wall injection of millimeter-sized bubbles. *Intl J. Heat Mass Transfer* **113**, 1200–1211.

KITAGAWA, A., KITADA, K. & HAGIWARA, Y. 2010 Experimental study on turbulent natural convection heat transfer in water with sub-millimeter-bubble injection. *Exp. Fluids* **49**, 613–622.

KITAGAWA, A. & MURAI, Y. 2013 Natural convection heat transfer from a vertical heated plate in water with microbubble injection. *Chem. Engng Sci.* **99**, 215–224.

KOLMOGOROV, A.N. 1991 The local structure of turbulence in incompressible viscous fluid for very large Reynolds numbers. *Proc. Math. Phys. Eng. Sci.* **434** (1890), 9–13.

KURE, I.K., JAKOBSEN, H.A. & SOLSVIK, J. 2024 Experimental study of interfacial mass transfer from single CO_2 bubbles ascending in stagnant water. *Chem. Engng Sci.* **287**, 119684.

KWAKKEL, M., BREUGEM, W.P. & BOERSMA, B.J. 2013 Extension of a CLSVOF method for droplet-laden flows with a coalescence/breakup model. *J. Comput. Phys.* **253**, 166–188.

LAKKARAJU, R., STEVENS, R.J.A.M., ORESTA, P., VERZICCO, R., LOHSE, D. & PROSPERETTI, A. 2013 Heat transport in bubbling turbulent convection. *PNAS* **110** (23), 9237–9242.

LANDAU, L.D. & LIFSHITZ, E.M. 1987 *Fluid Mechanics*, vol. 6. Elsevier.

LEE, I., CHANG, J., KIM, K. & CHOI, H. 2024 A numerical study on the turbulence characteristics in an air–water upward bubbly pipe flow. *J. Fluid Mech.* **994**, A10.

LEE, J.H., KIM, H., LEE, J. & PARK, H. 2021 Scale-wise analysis of upward turbulent bubbly flows: an experimental study. *Phys. Fluids* **33** (5), 053316.

LEONARDI, S., ORLANDI, P., DJENIDI, L. & ANTONIA, R.A. 2015 Heat transfer in a turbulent channel flow with square bars or circular rods on one wall. *J. Fluid Mech.* **776**, 512–530.

LIENHARD IV, J.H. & LIENHARD V, J.H. 2005 *A Heat Transfer Textbook*. Phlogistron.

LIU, T.J. 1993 Bubble size and entrance length effects on void development in a vertical channel. *Intl J. Multiphase Flow* **19** (1), 99–113.

LOISY, A., NASO, A. & SPELT, P.D.M. 2018 The effective diffusivity of ordered and freely evolving bubbly suspensions. *J. Fluid Mech.* **840**, 215–237.

LOU, W. & ZHU, M. 2016 Numerical simulations of non-metallic inclusions behavior in gas-stirred ladle. In *Proceedings of the 8th Pacific Rim International Congress on Advanced Materials and Processing*, pp. 3149–3156. Springer International Publishing.

LU, J., BISWAS, S. & TRYGGVASON, G. 2006 A DNS study of laminar bubbly flows in a vertical channel. *Intl J. Multiphase Flow* **32** (6), 643–660.

LU, J., FERNÁNDEZ, A. & TRYGGVASON, G. 2005 The effect of bubbles on the wall drag in a turbulent channel flow. *Phys. Fluids* **17** (9), 095102.

LU, J. & TRYGGVASON, G. 2007 Effect of bubble size in turbulent bubbly downflow in a vertical channel. *Chem. Engng Sci.* **62** (11), 3008–3018.

LU, J. & TRYGGVASON, G. 2018 Direct numerical simulations of multifluid flows in a vertical channel undergoing topology changes. *Phys. Rev. Fluids* **3**, 084401.

LU, J. & TRYGGVASON, G. 2019 Multifluid flows in a vertical channel undergoing topology changes: Effect of void fraction. *Phys. Rev. Fluids* **4**, 084301.

LU, M., YANG, Z. & DENG, B. 2025 Numerical study of turbulent bubbly upflow: effect of density ratio. *J. Fluid Mech.* **1007**, A63.

MANGANI, F., SOLIGO, G., ROCCON, A. & SOLDATI, A. 2022 Influence of density and viscosity on deformation, breakage, and coalescence of bubbles in turbulence. *Phys. Rev. Fluids* **7**, 053601.

MARCHIORO, M., TANKSLEY, M. & PROSPERETTI, A. 1999 Mixture pressure and stress in disperse two-phase flow. *Intl J. Multiphase Flow* **25** (6), 1395–1429.

MAZZITELLI, I.M., LOHSE, D. & TOSCHI, F. 2003 On the relevance of the lift force in bubbly turbulence. *J. Fluid Mech.* **488**, 283–313.

MOIN, P. & VERZICCO, R. 2016 On the suitability of second-order accurate discretizations for turbulent flow simulations. *Eur. J. Mech. B Fluids* **55**, 242–245.

MUKHERJEE, S., SAFDARI, A., SHARDT, O., KENJEREŠ, S. & VAN DEN AKKER, H.E.A. 2019 Droplet-turbulence interactions and quasi-equilibrium dynamics in turbulent emulsions. *J. Fluid Mech.* **878**, 221–276.

NA, Y., PAPAVASSILIOU, D.V. & HANRATTY, T.J. 1999 Use of direct numerical simulation to study the effect of Prandtl number on temperature fields. *Intl J. Heat Fluid Flow* **20** (3), 187–195.

NI, R. 2024 Deformation and breakup of bubbles and drops in turbulence. *Annu. Rev. Fluid Mech.* **56**, 319–347.

NIÑO, L., GELVES, R. & SOLSVIK, J. 2023 Viscous effects on gas–liquid hydrodynamics for bubble size determinations in different Newtonian and non-Newtonian fluids using a CFD–PBM model. *Chem. Engng Sci.* **282**, 119324.

ORLANDI, P. 2012 *Fluid Flow Phenomena: A Numerical Toolkit*. Springer Dordrecht.

ORLANDI, P., SASSUN, D. & LEONARDI, S. 2016 Dns of conjugate heat transfer in presence of rough surfaces. *Intl J. Heat Mass Transfer* **100**, 250–266.

PANDA, A., WEITKAMP, Y.E.J., RAJKOTWALA, A.H., PETERS, E.A.J.F., BALTUSSEN, M.W. & KUIPERS, J.A.M. 2019 Influence of gas fraction on wall-to-liquid heat transfer in dense bubbly flows. *Chem. Engng Sci. X* **4**, 100037.

PEETERS, J.W.R. & SANDHAM, N.D. 2019 Turbulent heat transfer in channels with irregular roughness. *Intl J. Heat Mass Transfer* **138**, 454–467.

PERUMANATH, S., BORG, M.K., CHUBYNSKY, M.V., SPRITTLES, J.E. & REESE, J.M. 2019 Droplet coalescence is initiated by thermal motion. *Phys. Rev. Lett.* **122**, 104501.

PICANO, F., BREUGEM, W.-P. & BRANDT, L. 2015 Turbulent channel flow of dense suspensions of neutrally buoyant spheres. *J. Fluid Mech.* **764**, 463–487.

PILLER, M., NOBILE, E. & HANRATTY, T.J. 2002 DNS study of turbulent transport at low Prandtl numbers in a channel flow. *J. Fluid Mech.* **458**, 419–441.

PIROZZOLI, S. 2023 Prandtl number effects on passive scalars in turbulent pipe flow. *J. Fluid Mech.* **965**, A7.

PIROZZOLI, S., BERNARDINI, M. & ORLANDI, P. 2016 Passive scalars in turbulent channel flow at high Reynolds number. *J. Fluid Mech.* **788**, 614–639.

PIROZZOLI, S. & ORLANDI, P. 2021 Natural grid stretching for DNS of wall-bounded flows. *J. Comput. Phys.* **439**, 110408.

POPE, S.B. 2000 *Turbulent Flows*. Cambridge University Press.

POPINET, S. 2009 An accurate adaptive solver for surface-tension-driven interfacial flows. *J. Comput. Phys.* **228** (16), 5838–5866.

PROCACCI, D., AROSEMENA, A.A., DI GIORGIO, S. & SOLSVIK, J. 2026 Turbulence anisotropy modulation in bubble-laden channel flow: a numerical study. *Intl J. Multiphase Flow* **195**, 105505.

PROCACCI, D., ROCCON, A., SOLSVIK, J. & SOLDATI, A. 2025 Heat transfer in drop-laden low-Prandtl-number channel turbulence. *J. Fluid Mech.* **1015**, A19.

PROSPERETTI, A. & TRYGGVASON, G. 2007 *Computational Methods for Multiphase Flow*. Cambridge University Press.

RAVELET, F., COLIN, C. & RISSO, F. 2011 On the dynamics and breakup of a bubble rising in a turbulent flow. *Phys. Fluids* **23** (10), 103301.

RAVISANKAR, M. & ZENIT, R. 2024 Velocity fluctuations for bubbly flows at small Re. *J. Fluid Mech.* **1001**, A34.

REYNOLDS, O. 1874 On the extent and action of the heating surface of stream boilers. *Proc. Lit. Soc. Manchester* **14**, 7–12.

RIBOUX, G., RISSO, F. & LEGENDRE, D. 2010 Experimental characterization of the agitation generated by bubbles rising at high Reynolds number. *J. Fluid Mech.* **643**, 509–539.

RISSO, F. 2016 Physical interpretation of probability density functions of bubble-induced agitation. *J. Fluid Mech.* **809**, 240–263.

ROCCON, A. 2025 Boiling heat transfer by phase–field method. *Acta Mech.* **236**, 5623–5638.

ROCCON, A., ZONTA, F. & SOLDATI, A. 2023 Phase-field modeling of complex interface dynamics in drop-laden turbulence. *Phys. Rev. Fluids* **8**, 090501.

ROSSI, D., DI GIORGIO, S. & PIROZZOLI, S. 2025 Comparative analysis of volume of fluid and phase–field methods for numerical simulations of two-phase flows. *Intl J. Multiphase Flow* **189**, 105245.

SANTARELLI, C., ROUSSEL, J. & FRÖHLICH, J. 2016 Budget analysis of the turbulent kinetic energy for bubbly flow in a vertical channel. *Chem. Engng Sci.* **141**, 46–62.

SERIZAWA, A., KATAOKA, I. & MICHIYOSHI, I. 1975 Turbulence structure of air–water bubbly flow–II. Local properties. *Intl J. Multiphase Flow* **2** (3), 235–246.

SHU, C.-W. & OSHER, S. 1989 Efficient implementation of essentially non-oscillatory shock-capturing schemes, ii. *J. Comput. Phys.* **83** (1), 32–78.

SILVI, L.D., CHANDRAKER, D.K., GHOSH, S. & DAS, A.K. 2021 Understanding dry-out mechanism in rod bundles of boiling water reactor. *Intl J. Heat Mass Transfer* **177**, 121534.

SÖDER, M., JÖNSSON, P. & JONSSON, L. 2004 Inclusion growth and removal in gas-stirred ladles. *Steel Res. Intl* **75** (2), 128–138.

SOLIGO, G., ROCCON, A. & SOLDATI, A. 2019a Breakage, coalescence and size distribution of surfactant-laden droplets in turbulent flow. *J. Fluid Mech.* **881**, 244–282.

SOLIGO, G., ROCCON, A. & SOLDATI, A. 2019b Coalescence of surfactant-laden drops by phase field method. *J. Comput. Phys.* **376**, 1292–1311.

TANAKA, M. 2011 Numerical study on flow structures and heat transfer characteristics of turbulent bubbly upflow in a vertical channel. In *Computational Simulations and Applications* (ed. J. Zhu), chap. 5. IntechOpen.

TOKUHIRO, A.T. & LYKOUDIS, P.S. 1994 Natural convection heat transfer from a vertical plate–i. Enhancement with gas injection. *Intl J. Heat Mass Transfer* **37** (6), 997–1003.

TOMIYAMA, A. 1998 Struggle with computational bubble dynamics. *Multiphase Sci. Technol.* **10** (4), 369–405.

TOMIYAMA, A., TAMAI, H., ZUN, I. & HOSOKAWA, S. 2002 Transverse migration of single bubbles in simple shear flows. *Chem. Engng Sci.* **57** (11), 1849–1858.

TRYGGVASON, G., SCARDOVELLI, R. & ZALESKI, S. 2011 *Direct Numerical Simulations of Gas–Liquid Multiphase Flows*. Cambridge University Press.

WANG, S.K., LEE, S.J., JONES, O.C. & LAHEY, R.T. 1987 3-d turbulence structure and phase distribution measurements in bubbly two-phase flows. *Intl J. Multiphase Flow* **13** (3), 327–343.

WANG, Y., CAO, L., VANIERSCHOT, M., CHENG, Z., BLANPAIN, B. & GUO, M. 2020 Modelling of gas injection into a viscous liquid through a top-submerged lance. *Chem. Engng Sci.* **212**, 115359.

WEYMOUTH, G.D. & YUE, D.K.P. 2010 Conservative volume-of-fluid method for free-surface simulations on cartesian-grids. *J. Comput. Phys.* **229** (8), 2853–2865.

WHITE, F.M. & MAJDALANI, J. 2006 *Viscous Fluid Flow*. McGraw-Hill New York.

WU, J.-S. & FAETH, G.M. 1994 Sphere wakes at moderate Reynolds numbers in a turbulent environment. *AIAA J.* **32** (3), 535–541.

XU, Y., ERSSON, M. & JÖNSSON, P.G. 2016 A numerical study about the influence of a bubble wake flow on the removal of inclusions. *ISIJ Intl* **56** (11), 1982–1988.

YANG, H., XING, Y., SUN, L., CAO, Y. & GUI, X. 2020*a* Kinetics of bubble-particle attachment and detachment at a single-bubble scale. *Powder Technol.* **370**, 251–258.

YANG, W., LUO, Z., GU, Y., LIU, Z. & ZOU, Z. 2020*b* Simulation of bubbles behavior in steel continuous casting mold using an Euler-Lagrange framework with modified bubble coalescence and breakup models. *Powder Technol.* **361**, 769–781.

ZHANG, L. & TANIGUCHI, S. 2000 Fundamentals of inclusion removal from liquid steel by bubble flotation. *Intl Mater. Rev.* **45** (2), 59–82.

ZHANG, Q. & PROSPERETTI, A. 2010 Physics-based analysis of the hydrodynamic stress in a fluid-particle system. *Phys. Fluids* **22** (3), 033306.